Faculty of Physics and Astronomy

University of Heidelberg

Diploma thesis

in Physics

submitted by

Stefan Weis

born in Heilbronn

November 2007

Setup of a Laser System for Ultracold Sodium –

Towards a Degenerate Gas of Ultracold Fermions

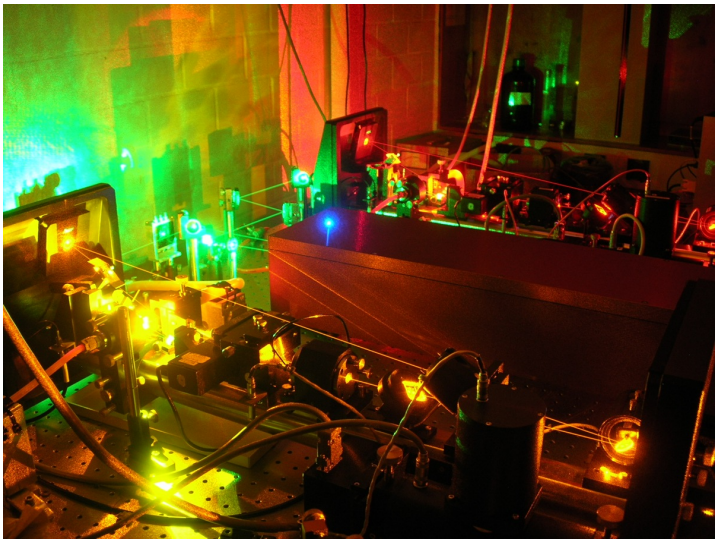

This diploma thesis has been carried out by Stefan Weis at the

Kirchhoff Institute for Physics

under the supervision of

Prof. Dr. M. K. Oberthaler

Aufbau eines Natrium-Lasersystems zur Erzeugung ultrakalter, entarteter Fermigase

In dieser Diplomarbeit wird ein neuer Aufbau zur Erzeugung ultrakalter Natrium- und Lithiumgase vorgestellt. Ziel dieses Experiments ist die Herstellung entarteter Fermigase aus fermionischen ^{6}Li-Atomen, die mittels bosonischer ^{23}Na-Atome sympathetisch gekühlt werden. Dafür wurde das Natrium-Lasersystem entworfen und installiert. Ein wichtiger Schritt war die Implementierung einer magneto-optischen Falle für Natrium. In dieser Arbeit soll der bisherige Aufbau beschrieben und eine Einführung in die Thematik der ultrakalten, entarteten Fermigase gegeben werden.

Setup of a Laser System for Ultracold Sodium – Towards a Degenerate Gas of Ultracold Fermions

This thesis presents the first part of a new experimental setup for ultracold ^{23}Na and ^{6}Li gases. The aim of this experiment is to achieve Fermi degeneracy within a sample of fermionic ^{6}Li atoms. A laser system for bosonic ^{23}Na has been designed and set up. As a first experimental result a magneto-optical trap for sodium has been achieved. This diploma thesis describes the apparatus set up so far and gives an introduction to the field of ultracold, degenerate Fermi gases.

March
2007

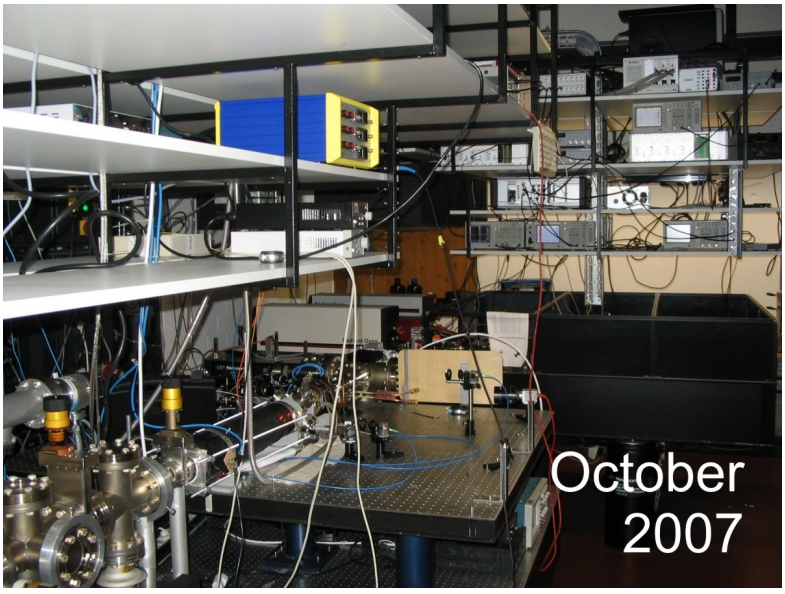
October
2007

Contents

1 Introduction **1**

1.1 Quantum Statistics - Bosons and Fermions 1
1.2 Degenerate Fermions 4
1.2.1 Feshbach Resonances 4
1.2.2 Theoretical Approaches 7
1.2.2.1 BEC Theory 7
1.2.2.2 Strongly Coupled Fermions 8
1.2.3 Current Research Topics - A Short Summary 9
1.3 Why Lithium **AND** Sodium? 9
1.3.1 General Aspects 10
1.3.2 Our Motivation for Choosing Lithium and Sodium 11
1.4 Outline 11

2 Theory **13**

2.1 Dye Lasers 13
2.1.1 Some Laser Basics 13
2.1.2 The Ring Dye Laser 15
2.1.3 Singlemode Operation of Dye Lasers 18
2.1.3.1 Optical Diode (OD) and Thin Quartz Plate 19
2.1.3.2 Selecting a Longitudinal Mode 20
2.1.3.3 Birefringent Filter (BR) 20
2.1.3.4 Thin and Thick Etalon (TNE and TKE) 22
2.1.3.5 Tuning Resonator Modes: Galvo/Brewster Plate and Tweeter (GP and M2) 23
2.1.3.6 Locking the Laser to the Internal Fabry-Perot Cavity and Frequency Sweeps 24
2.2 Magneto-Optical Trapping 25
2.2.1 Light Forces on Two-Level Atoms 25

2.2.1.1 Dipole Force . . . 26
2.2.1.2 Light Pressure Force . . . 27
2.2.2 Optical Molasses . . . 27
2.2.3 Magneto-Optical Trapping of Multilevel Atoms . . . 28
2.2.4 Sub-Doppler Cooling . . . 30
2.2.5 Repumping . . . 31
2.2.6 Limitations and the Dark Spot MOT for Sodium . . . 31

3 Experimental Setup **33**
3.1 Introduction . . . 33
3.2 Vacuum System . . . 34
3.2.1 The Vacuum Chamber . . . 34
3.2.2 Pumping . . . 35
3.3 Zeeman Slower . . . 35
3.3.1 Design Criteria . . . 36
3.3.2 The Setup and a Basic Introduction . . . 36
3.4 Magnetic Fields . . . 38
3.4.1 Feshbach Coils . . . 38
3.4.2 Magnetic Trap . . . 39
3.5 The Laser System . . . 40
3.5.1 Why Dye Lasers? . . . 40
3.5.2 Frequencies . . . 40
3.5.2.1 Locking the Laser to an Atomic Resonance . . . 41
3.5.2.2 MOT . . . 42
3.5.2.3 MOT Repumper . . . 43
3.5.2.4 Zeeman Slower . . . 43
3.5.2.5 Zeeman Slower Repumper . . . 44
3.5.2.6 Imaging . . . 44
3.5.2.7 Transfer into a Magnetic Trap . . . 44
3.5.3 Frequency Generation . . . 45
3.5.4 The MOT setup . . . 47
3.5.4.1 Repumping Light for Sodium and the Dark Spot MOT . . . 47

4 First Measurements **51**
4.1 A Provisional Absorption Imaging System . . . 51
4.1.1 Optical Density of an Atomic Cloud and the Beer-Lambert Law . . . 51
4.1.2 A Provisional Imaging System . . . 53

4.2 Estimating the Atom Number in the Sodium MOT 54

5 Résumé and Outlook **57**
5.1 Current Progress of the Experiment 57
5.2 Outlook 57

A Sodium Data **59**

B Atomic Beam Shutter **61**
B.1 General Aspects 61
B.2 User Manual 61
B.2.1 Installation 61
B.2.2 Choosing Setpoints and Operation 62
B.3 The Circuit 62
B.4 Programming 62
B.5 Source Code 64

C Beam Profiler **67**
C.1 Application Notes 67
C.1.1 Warnings 67
C.2 Functionality 68
C.2.1 Overview, Graphs and Fitting 68
C.2.2 Reducing Stripes and Saving Results 68
C.3 Some Comments on the Programming and Fitting 69

D Spectroscopy Cell and Doppler-Free Laser Locking **71**
D.1 The Spectroscopy Cell 71
D.2 Lock-in Scheme 72

E RF-Drivers for High-Frequency Components **75**

F Danksagung **77**

1 Introduction

1.1 Quantum Statistics - Bosons and Fermions

Every particle - elementary or composite - can be attributed to one of two groups. It can either be a boson or a fermion. Let us take a look at figure 1.1. On the left hand side, a schematic of a gas at say room temperature in a harmonic trap is shown. In quantum mechanics the eigenstates of such a trap can now be calculated yielding equally spaced energy levels for a one-dimensional model, indicated by the horizontal lines. For a classical gas the available states are sparsely populated according to the Boltzmann distribution given by:

$$N_i = \frac{1}{Z} e^{-E_i/k_B T} \tag{1.1}$$

where N_i denotes the number of particles within a sample in the i-th state with an eigenenergy of E_i at temperature T in a sample of $N = \sum_i N_i$ atoms. Z is some normalization constant (in statistical mechanics: partition function) and k_B is Boltzmann's constant.

Cooling this sample down to very low temperatures while at the same time increasing the density will, at some point, lead to the appearance of quantum properties. For bosons the probability for the common occupation of one single state is increased compared to classical particles, satisfying the Bose-Einstein distribution given in equation (1.2), where μ denotes the chemical potential.

$$N_i = \frac{1}{e^{(E_i-\mu)/k_B T} - 1} \tag{1.2}$$

This enhancement leads to a macroscopic occupation of the ground state for high phase space densities, i.e. low temperatures paired with high densities. This phase is called Bose-Einstein condensate (BEC) and has been predicted as early as in 1924 by Satyendranath Bose and Albert Einstein [1, 2, 3]. In 1995 finally the first

pure[1] BECs have been realized experimentally by Eric Cornell and Carl Wieman at JILA [4] and Wolfgang Ketterle at MIT [5].

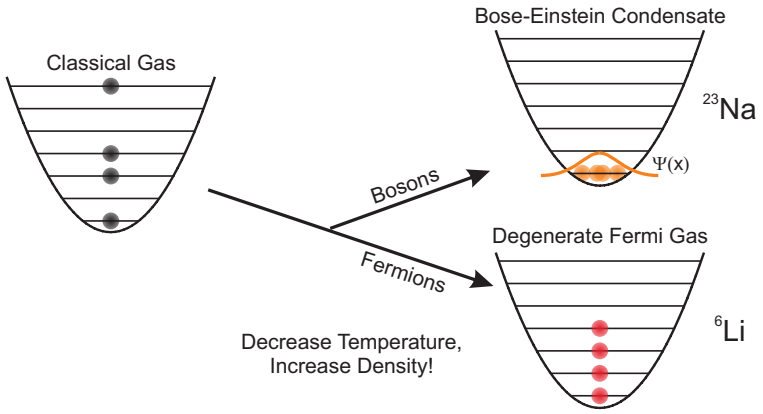

Figure 1.1: Cooling down a gas leads to the appearance of quantum properties. See text for more details.

Fermions on the other hand must not occupy one single quantum mechanical state. This is manifest in the Fermi-Dirac distribution, the analog to the aforementioned Bose-Einstein statistics:

$$N_i = \frac{1}{e^{(E_i-\mu)/k_BT}+1} < 1 \tag{1.3}$$

This has first been claimed by W. Pauli in 1925, known as Pauli's principle. Ultimately the fermions will reduce the system's energy when cooled down by occupying the lowest empty states available. This leads to a sharp transition between occupied and empty states at a certain energy level, known as the Fermi energy. This phase is referred to as a degenerate Fermi gas.

There are two more essential principles for an understanding of quantum gases. First in 1940 Wolfgang Pauli could show that the spin of a particle determines its quantum properties [6]. Bosons carry integer spin, whereas fermions have half-integer spin. The behavior of atoms as a whole is determined by the number of electrons, protons and neutrons in its nucleus and shell, each contributing spin 1/2. Thus for odd numbers like in ^{6}Li $(3+3+3)$ atoms are fermionic and for even numbers like in ^{23}Na $(11+11+12)$ they show bosonic behavior. Second, in

[1] The transition to the superfluid phase of ^{4}Heor type I superconductivity are Bose-Einstein condensed systems, but strong interactions between particles complicate these systems heavily. Strong interactions result in a reduced fraction of condensed atoms (about 10% in superfluid ^{4}He).

a regime in which quantum properties play a role, particles do no longer behave like classical point-like particles but also show wave-like properties. This was first postulated in 1924 by L.V. de Broglie who attributed a wavelength

$$\lambda_{dB} = \frac{h}{p} \tag{1.4}$$

to a particle of momentum p [7]. These properties are only relevant if the inner structure of the particle is small compared to its wavelength, since otherwise particle-particle interactions are mainly arising from the interaction of electronic shells. A second point is, that the inter-atomic distance needs to be on the order of this wavelength. Or in other words:

$$n\lambda_{dB}^3 > 1 \tag{1.5}$$

where n is the number density. In statistical quantum mechanics this product is also called phase space density or degeneracy parameter. This already gives a rough estimate for temperatures needed in a system of given number density n to observe effects arising mainly from quantum statistics. Therefore, we are inserting equation (1.4) into equation (1.5). Using that the particle density n in an ideal gas is given by $n = P/(k_B T)$, where P denotes the pressure, yields a critical temperature on the order of:

$$T_C \approx \frac{h^2 n^{2/3}}{2mk_B} \tag{1.6}$$

This temperature is referred to as critical temperature for bosons[2] and Fermi temperature for fermions. Yet for a first estimate equation (1.6) is sufficient. Typical densities in experiments with cold atoms are on the order of $10^{14}\,\mathrm{atoms/cm^3}$. The molar mass of ^{6}Li is $6\,\mathrm{g/mol}$. This yields temperatures on the order of $1\,\mu K$. Comparing this to a degenerate gas of electrons in a metal gives rise to a factor of 10^4 (mass ratio) plus another six orders of magnitude (density ratio $\approx 10^{9 \cdot 2/3}$), thus an overall factor of about 10^{10} in temperature, equivalent to temperatures on the order of 10000K! So one could ask: Why should one be interested in such hard-to-create systems? We would like to motivate this in the next section.

[2] A more accurate analysis yields another factor of 2.612 in phase space density for spinless atoms, resulting in temperatures that are about a factor of two lower. Corrections due to interactions turn out to be small.

1.2 Degenerate Fermions

Bose-Einstein condensation has been a very active field of research during the last 12 years. In the meantime there are approximately 60 BEC experiments in the world[3] that have accumulated extended knowledge about laser and evaporative cooling, interactions in ultracold samples and BECs in a wealth of different geometries and potentials. BECs have been put into double-wells [8, 9], lattices [10], effective two-dimensional structures [11], have been rotated [12] ... Yet there is still a lot of exciting physics to be done. Common to them all is, that these systems can be well described theoretically as described briefly in section 1.2.2.

One research area that has developed recently and that we would like to join, is the creation of degenerate Fermi gases of neutral atoms (DG). The first such DG gas has been observed in the group of Deborah Jin at JILA in Boulder in 1999 [13, 14]. Since then, several groups have caught up. A short overview on current research topics and involved groups will be given in section 1.2.3.

There are now various reasons making research on DG so exciting. Ultracold degenerate Fermi gases are a model system for nearly any strongly correlated fermionic system. Quarks in a quark-gluon plasma, electrons in solids or neutron stars may serve as examples. These systems have in common that many aspects have not yet been captured theoretically and only now theorists are developing methods that are able to treat many-body systems of fermions since perturbation theories break down in this case (refer to section 1.2.2 for some remarks on this). An important advantage of such a system is that it is clean. Clean in this context means that no perturbing interactions like for example in solids exist. There are no electron-phonon interactions, no electrostatic interactions among electrons and with the ionic cores of the lattice. However, the most important thing is that within a sample of trapped ultracold fermions there are several tunable parameters that do not exist in other systems such as density (by means of the restoring force within the trap), temperature (one can stop cooling at any point), and even scattering lengths. The latter has the most dramatic consequences and will be discussed in the following.

1.2.1 Feshbach Resonances

Consider a sample of atoms containing different spin states[4] of fermions. A priori collisions between two atoms with different spin states will only happen if they

[3] Source: `http://www.uibk.ac.at/exphys/ultracold/atomtraps.html`

[4] We will come back to that point in section 1.3.

approach each other to some distance comparable to the diameter of the atoms (i.e. several $a_0 \approx 5 \cdot 10^{-11}\,\mathrm{m}$, Bohr radius), that is much smaller than the inter-atomic distance (about 100 nm) in an ultracold gas. Thus collisions will happen only rarely.

This changes drastically if a magnetic field is applied and tuned in the vicinity of a so-called Feshbach resonance [15]. These resonances lead to scattering lengths a that exceed by far the geometric extensions of the bare atoms. In figure 1.2 a plot of the Feshbach resonances for a pair of ^{6}Li atoms of opposite spin is given. There are two known Feshbach resonances at relatively low magnetic fields, a very narrow one at 543 G and a very broad one at 837 G. The latter will be used in our experiment since it demands only little accuracy when ramping magnetic fields. Moreover one can even choose whether the particles effectively attract ($a < 0$) or repel ($a > 0$) each other.

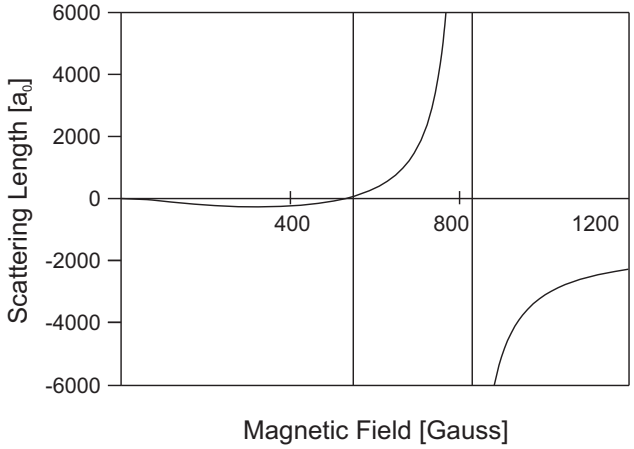

Figure 1.2: Scattering length a in units of the Bohr radius a_0 for ^{6}Li atoms with opposite spin as a function of the magnetic field [16]. There are two Feshbach resonances, at 543 G (not resolved in this plot) and 837 G, and a zero crossing of the scattering length at 528G for the two lowest hyper-fine states in high fields. For $a > 0$ the interaction is repulsive, otherwise attractive.

We cannot give a detailed introduction to Feshbach resonances in this work, so let us just motivate where they are arising from. For a nice introduction refer to [17].

In figure 1.3 potential curves for two molecular states of different total angular momentum (e.g. lowest two hyper-fine states in high field) as a function of the inter-atomic distance are plotted. The dashed line corresponds to the kinetic energy of the unbound particles in the center of mass system. The offset arises from

the different hyper-fine states in the molecule. Different magnetic moments of the two spin states allow for shifting the upper potential curve relative to the lower one. Preparing the atoms in the open channel (the lower curve), i.e. in an unbound state yields a coupling to the closed channel (upper curve) by means of spin exchange collisions of the nuclear spin. If ever the kinetic energy is close to an energy level of the closed channel the eigenstates repel each other (avoided transitions), leading to a drastically increased scattering length[5]. Thereby a lowering (increase) in energy is equivalent to an attractive (a repulsive) interaction.

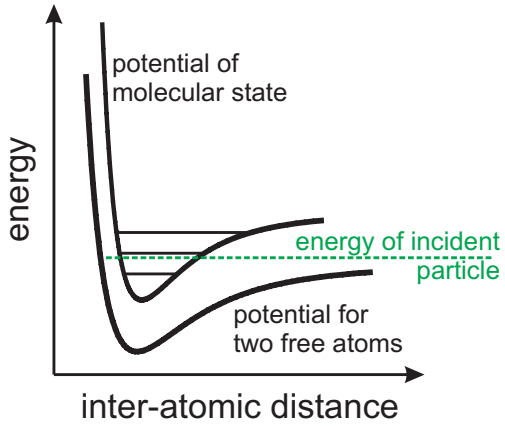

Figure 1.3: Schematic of potential curves for two molecular states of different total angular momentum as a function of the inter-atomic distance; *dashed line:* kinetic energy of the involved particles in the center of mass system.

At sufficiently low temperature this leads either to Cooper pairing (for negative scattering lengths) or molecule formation (for positive scattering lengths). This situation is often referred to as BEC-BCS cross-over, since on the one side of the resonance molecules are condensed into a molecular BEC (described by BEC theory) on the other side bosonic Cooper pairs described in the BCS[6]-theory of superconductors.

For completeness we mention that there are also Feshbach resonances for p-wave scattering of two atoms in the same spin state [19].

[5] This system can be treated similarly to an atom in a light field, using a dressed state approach [17]. See also [18] for a nice introduction.

[6] Bardeen, Cooper and Schrieffer

1.2.2 Theoretical Approaches

1.2.2.1 BEC Theory

The inner structure (electronic configuration, magnetic and electrostatic properties) of species usually used in cold atom experiments is well known. Using this knowledge collisions involving two atoms can be described theoretically. In cold atom experiments with atomic velocities on the order of millimeters per second the collisional energies are weak compared to the binding energies of the innermost shells. Thus only valence electrons contribute. Two-particle interaction - featuring scattering and formation of molecules - of atoms is well understood and the Schrödinger equation can be solved numerically.

However, moving to higher atom numbers quickly exceeds any available computer powers. Furthermore already three classical(!) particles (e.g. two planets in a solar system[20]) may behave chaotically and solving such problems exactly is impossible. On the other hand the exact solution of the Schrödinger equation of say 10^6 cold atoms cannot be examined in an experiment anyway. One is rather interested in macroscopic quantities that can be determined in an experiment like for example densities, temperature, correlations between observables or maybe the distance and radius of vortices in a superfluid system.

As discussed before, bosons in a BEC occupy the same quantum mechanical state. Thus a simple and widely used approach is to reduce the N particle Schrödinger equation to an effective one-particle one in a mean-field approach:

$$i\hbar\frac{\partial}{\partial t}\Psi(\vec{r},t) = \left[-\frac{\hbar^2}{2m}\Delta + V_{ext}(\vec{r}) + g\left|\Psi(\vec{r},t)\right|^2\right]\Psi(\vec{r},t) \tag{1.7}$$

Here V_{ext} denotes some external potential, N is the particle number and g is the coupling constant that is proportional to the scattering length, thus positive for repulsive and negative for attractive interactions. Mean-field in this context means that one assumes the other atoms to be homogeneously distributed in space, creating a net background field corresponding to the last term of the Hamiltonian. This equation was first derived by Gross [21, 22] and Pitaevskii [23] in 1961 and is called **Gross-Pitaevskii equation** (GPE). The non-linear term in the Hamiltonian assumes the interaction of the particles to be point-like. Only two-body s-wave scattering processes are taken into account. This is justified if the temperature is low enough and higher order scattering freezes out and if the inter-atomic distance is big compared to the scattering length such that three-body collisions do not occur. For attractive interaction the non-linear term will decrease the total energy of the system and thus lead to an increased particle density[7] n and vice

[7] Note that $n \propto |\Psi(\vec{r},t)|^2$, where n is the particle density.

versa. Using this, many phenomena can be described in Bose-Einstein condensed systems. If needed, higher order interactions can be integrated into this model.

1.2.2.2 Strongly Coupled Fermions

A more interesting point and a currently very active field of research is the description of strongly coupled fermionic systems. Evidently, an approach similar to the GPE can not exist, since fermions have to occupy orthogonal quantum mechanical states with an overall antisymmetric wave function. As long as they are weakly interacting perturbation theoretical approaches still hold. However, the most exciting physics takes place right on and next to Feshbach resonances where the systems are strongly interacting. Directly on a Feshbach resonance the scattering length diverges and systems are supposed to show a unitary behavior, i.e. they show the same characteristics on all length scales (in quark-gluon plasma but also in neutron stars).

One method currently developed at the Theoretical Institute of the University of Heidelberg [24, 25] is a quantum field theoretical approach called **Functional Renormalization** (FR). In quantum field theory [26] one typically encounters divergences for high momenta (i.e. small distances). These arise from a breakdown of the continuum description of fields[8]. However, this problem can be solved by introducing a so-called ultraviolet cutoff and replacing higher momentum physics by measured quantities. For quantum field theory a small number of measured quantities like for example the electron's mass and charge are needed. However, this allows for quantitative predictions of physical observables. Whenever such an approach is feasible, the corresponding theory is called renormalizable. In a next step, the known action on a microscopic scale is extended to an effective action on a macroscopic scale. Since FR is not based on perturbation theory it can be used for the description of strongly correlated systems. The outstanding point about ultracold gases is now, that the microscopic behavior of these atoms is very well known - in contrast to for example in high energy physics. Taking this as a starting point and extending this to a macroscopic scale yields macroscopic observables (e.g. relations between correlation lengths and core sizes of vortices).

A complementary method is **Quantum Monte-Carlo simulation**. See [27] for a very detailed review and [28] for a more recent example on degenerate Fermi gases close to a Feshbach resonance. Basically, one uses some quantum mechanical model (e.g. many-body Schrödinger equation, path integral formalism) as a starting point and defines some initial wavefunction. Then random walks are used

[8] This is in some way comparable to the UV catastrophe in Rayleigh-Jean's law, where a discrete description needs to be applied for high photon momenta.

for solving (path) integrals or for consecutive steps in phase space.

1.2.3 Current Research Topics - A Short Summary

In this section we would like to give a short overview on current research topics in the leading groups of the international community. This list does not claim to be complete.

- In the group of **Deborah Jin** at *JILA* p-wave Feshbach resonances are examined [19].
- The groups of **Randy Hulet**, *Rice University* [29] and **Wolfgang Ketterle**, *MIT* [30] deal with imbalanced spin mixtures and explore phase diagrams in such systems.
- At *Duke University* the group of **John Thomas** investigates thermodynamics at a Feshbach resonance [31].
- The group of **Rudi Grimm**, *University of Innsbruck* is doing spectroscopy [32] on ultra-cold degenerate Fermi gases and examines their dynamics [33].
- In the group of **Christophe Salomon**, *ENS* the transition from a gaseous to a crystalline phase is investigated [34]. Recently expansion experiments have been done [35].

1.3 Why Lithium AND Sodium?

We have chosen fermionic ^{6}Li and bosonic ^{23}Na for our experiment. But why a bosonic part if all this is about fermions? Even though there is in fact interesting physics [36, 37] when dealing with a mixture of a degenerate Fermi gas and a BEC, this mainly has to do with our cooling strategy. In a first step laser cooling is done. Yet to reach temperatures below the critical temperatures this is not sufficient, since only temperatures on the order of hundreds of μK can be achieved for lithium. In BEC physics evaporative cooling [38] is done. Thereby the fastest atoms are removed. Efficient cooling is only achieved if collision induced rethermalization occurs sufficiently fast. These collisions are mainly s-wave scattering processes, since higher order collisions freeze out at the given temperatures. During this step the atoms are typically trapped in a magnetic trap[9], thus the sample is usually

[9]There are groups with "all optical" setups [39]. In this case atoms are transferred from the MOT to an optical dipole trap directly and this problem does not arise. But for this enormous laser powers (typically several tens of watts) are needed for achieving sufficiently high potentials.

spin polarized. The important point about spin-polarized fermions is now, that s-wave collisions are forbidden by Pauli's principle for low temperatures, while higher order collisions are freezing out. Consequently thermalization would slow down drastically for decreasing temperatures.

As collisions between different spin states are still allowed at low temperatures, cooling down to degeneracy can be done by using different spin states. In fact, this has been the first working solution ever and was chosen by the group of Deborah Jin at JILA. Disadvantageous is that one loses about 99% of the atoms. This can be circumvented using a second approach, called "sympathetic cooling" [40]. It is based on creating a conventional BEC of bosons and during this cooling process using the bosons as a refrigerant for the fermionic component. An important advantage is that the atom number of fermions decreases only slightly.

1.3.1 General Aspects

During the last few years several groups have already reached Fermi degeneracy with different approaches and various combinations of elements [14, 41, 42, 43]. This section is meant to be an overview on different isotopes used together with a brief discussion of their pros and cons.

Common to nearly all of these experiments is, that either ^{6}Li or ^{40}K are used[10]. Alkalis have in common that their level schemes are simple[11] and well understood. ^{6}Li and ^{40}K (half life time 10^9 years[12]) are the only stable alkaline fermionic isotopes. Both show Feshbach resonances (see section 1.2.1 for details on ^{6}Li) at reasonable magnetic fields. However, ^{6}Li offers a resonance with a width of about 100G whereas in ^{40}K the widths on the order of one Gauss can hardly be resolved [45]. Another point in favor of ^{6}Li is that molecules formed in the vicinity of a Feshbach resonance have higher lifetimes [46, 47]. On the other hand ^{40}K has a resolved hyper-fine structure in the excited state (thus better laser cooling is possible, see section 2.2.4). Advantageous about ^{40}K is also that its vapor pressure is much higher at a given temperature than for Lithium. The magneto-optical trap (cf. 2.2) can thus be loaded from the background pressure created by a small dispenser whereas a high temperature oven needs to be used for ^{6}Li.

Once the fermionic part is chosen, the choice of bosons is reduced taking into account that for optimal heat transfer, the masses of the two species should not

[10] Recently the group of Yoshiro Takahashi achieved Fermi degeneracy with (exotic) Ytterbium (Yb), offering two stable fermionic and five stable bosonic isotopes, all with reasonable natural abundance [44]. We will restrict our discussion to the aforementioned elements.

[11] They are hydrogen-like with only one electron in the outermost shell.

[12] data from `http://atom.kaeri.re.kr/ton/`

differ too much. The same condition holds for magnetic trapping (cf. section 3.4.2), as for different masses the centers of the trap for the different species are shifted slightly due to the gravitational force (also called gravitational sag). This impairs their heat contact. The bosonic counterpart should not be lighter than the fermions. As seen in equation (1.6) the critical temperature decreases for increasing mass. As a consequence, the deeper one wants to cool into degeneracy, the lighter the fermion should be relative to the boson. Additionally one needs a sufficiently large thermal bath, for the desired size and temperature of the fermionic sample. Finally, the inter-species collisional properties are of importance, however, they are generally not predictable and have to be acquired experimentally. Resuming the previous arguments, mainly four combinations are reasonable and used ^{7}Li / ^{6}Li (e.g. in the groups of Hulet, Rice and Salomon, ENS), ^{87}Rb / ^{40}K (e.g. in the groups of Bloch, Mainz and of Inguscio, Florence) and ^{7}Li / ^{23}Na (group of Ketterle, MIT) and ^{6}Li / ^{87}Rb (e.g. in the group of Zimmermann, Tübingen).

1.3.2 Our Motivation for Choosing Lithium and Sodium

We chose ^{6}Li mainly for its broad Feshbach resonance that can easily be resolved. So the creation of a sufficiently homogeneous magnetic field all over the entire atomic cloud is feasible. As a last point ^{6}Li is readily available[13].

^{23}Na was chosen because it is only slightly heavier (as discussed before) and the biggest BECs ever have been realized with sodium [48]. Our Zeeman slower can be used for both species with sufficient efficiency (see 3.3.1). Last but not least, there are successful experiments running with ^{23}Na and ^{6}Li [49]. So we will not have to deal with problems that have not been solved before as the target of the experiment is to reach degeneracy as soon as possible.

1.4 Outline

On our way towards a degenerate gas of ultracold ^{6}Li atoms and a BEC of ^{23}Na mainly a vacuum system and a laser system need to be set up. Atoms are evaporated in two high temperature ovens, slowed down, trapped and cooled using magnetic fields and lasers. For sodium there are no solid state lasers available at present and dye lasers need to be used. The outline of this thesis is as follows:

[13] The natural abundance of ^{6}Li is about 7%, whereas the rest is ^{7}Li , we use enriched lithium containing about 95% ^{6}Li ; The natural abundance of ^{40}K is only about 0.012% and is mainly won in nuclear power stations.

In chapter 2 we will give an introduction to dye lasers to an extent that seemed to be necessary to understand the specific properties - also problems - of our laser system. Another point we would like to touch upon in this chapter is some theory on magneto-optical trapping.

Chapter 3 will give an overview on what has been set up in the first year of this experiment. We will describe the vacuum system, the Zeeman slower and the magnetic coils briefly before giving a more extensive description of the laser system that has mainly been developed and set up under the author's responsibility during the first months.

In part 4 we will present first measurements of the properties of our magneto-optical trap for sodium atoms.

The appendix finally contains some sodium data and several important experimental tools realized during this diploma thesis - namely a beam profiler based on a webcam, a microcontroller based atomic shutter driver for our vacuum apparatus, the spectroscopy cell for Doppler-free saturated spectroscopy of sodium and the driver electronics for high frequency modulators.

2 Theory

2.1 Dye Lasers

We use a laser system based on two Radiant Dyes Dye Ring Lasers. For sodium and lithium we chose rhodamine 6G (R6G) and DCM (4-Dicyanomethylene-2-methyl-6-(p-dimethylaminostyryl)-4H-pyran) respectively. In the following we will concentrate on our laser for sodium, however, the results are generic for nearly all dyes. In section 2.1.1 some laser basics needed in the subsequent chapters are given. In section 2.1.2 some special features of dyes are discussed. Finally, in section 2.1.3 we will show how to achieve single mode operation of a dye laser at a desired wavelength, introducing the mode selective elements in a dye ring laser.

2.1.1 Some Laser Basics

This section is not meant to be a profound introduction to laser physics. The aim is to recall some laser basics that will be needed in the following. For further details refer to any standard text book, e.g. [50] for a general introduction, or [51, 52] for specific questions on dye lasers. The first working laser – a ruby laser – was built in 1960 by Theodore Maiman[1]. Six years later the first dye laser was invented by chance in the group of Fritz P. Schäfer [53]. Examining the saturation characteristics of cyanine, the reflectivity of about 4% of a polished cuvette was sufficient to enable lasing.

Prerequisite for the construction of a laser is an active medium amplifying incoming light coherently (i.e. same phase and wavelength). Therefore, a population inversion needs to be achieved, since only then stimulated emission dominates the absorption in the gain medium. This cannot be achieved in thermal equilibrium or in a system of only two levels[2], since Boltzmann's factor cannot exceed 1. In appropriate systems of three and four levels, this becomes possible. A key feature of

[1] see `http://www.pat2pdf.org/patents/pat3353115.pdf` for the original patent

[2] Strictly spoken this holds only on timescales bigger than the natural linewidth.

these media is, that the laser transition's lifetime, constituted of all non-coherent decay channels (spontaneous emission, non-radiative decay) is long compared to all other decay processes. Let us have a look directly at the level scheme of rhodamine 6G in picture 2.1, that will be discussed in some more detail in the next section. Refer to figure 2.1 for notations of the various lifetimes and states. Lifetimes τ_2 and τ_4 are on the order of picoseconds or even sub picoseconds (see next section for a brief justification) and very small compared to $\tau_3 \approx 0.1\,\mu$s. Thus, one can assume in a simple approach that all electrons excited to $\langle 2\rangle$ decay into $\langle 3\rangle$ instantaneously. In a first step pumping light excites electrons from the ground state $\langle 1\rangle$ to any sublevel of the excited state $\langle 2\rangle$[3]. Non-radiative transitions (induced by non-elastic collisions) populate the state $\langle 3\rangle$. There are now several decay paths. The most desirable is stimulated emission to some sublevel of the ground state $\langle 4\rangle$. Furthermore, spontaneous emission to the ground state or transitions to the triplet states may occur. In a last step electrons in energy level $\langle 4\rangle$ relax to the ground state $\langle 1\rangle$. Taking into account the absorption of the pump beam, stimulated emission and spontaneous emission as well as all non-radiative processes, one can establish rate equations allowing to calculate the lasing threshold (i.e. the pump power needed for lasing) and the time dependent behavior.

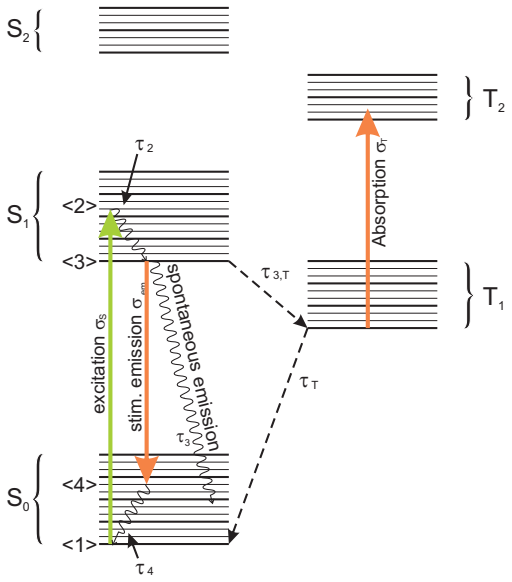

Figure 2.1: Term scheme of rhodamine 6G, S denotes electronic singlet states, T the corresponding triplet states

[3]Evidently $\langle 2\rangle$ and $\langle 4\rangle$ may be any state within the upper and lower band.

A last important property of dye lasers is, that in steady state operation dye lasers with electrons occupying only one single excited state (all electrons in $\langle 3 \rangle$) will run in a single longitudinal mode at every time (though fast mode hops may occur leading to an effective multi-mode operation). This is due to what is called homogeneous line broadening of the gain medium. Electrons in $\langle 3 \rangle$ serve as a reservoir for all possible longitudinal modes. As a consequence, only one mode at a time will be amplified at the expense of all the others. Stimulated emission within the gain medium amplifies the longitudinal mode with wavelength λ and intensity $I(\lambda)$ according to $\frac{dI(\lambda)}{dt} \propto N_3 \cdot I(\lambda)$, where N_3 denotes the density of electrons in the $\langle 3 \rangle$ state. Hence, the most intense mode depopulates electrons in the $\langle 3 \rangle$ state the most and prevails the others, that gain less gradually and get damped out by losses within the cavity. In case different longitudinal modes are amplified by different reservoirs of excited electrons, i.e. they do not compete, the gain media are called inhomogeneously broadened (for example Doppler broadening in gas lasers).

2.1.2 The Ring Dye Laser

In general, dye molecules consist of a large number of atoms. This leads to a big number of different vibrational degrees of freedom (50 atoms give rise to about 150 vibrational modes). Many of these vibronic excitations directly couple to the electronic transitions, adding sublevels to these spectra with typical mode spacings of approximately 1 THz to 100 THz. Additionally rotational degrees of freedom come into play with a mode spacing of typically 10 GHz to 1 THz. These levels are strongly broadened due to collisions with the solvent, yielding a quasi-continuous absorption spectrum. Furthermore, the band structure depends on temperature, dye concentration and acid-base equilibria with the molecules of the solvent.

There are mainly three generic classes of dye molecules (cf. figure 2.2). However, common to all of them is the presence of several conjugated double-bonds (a so called system of π-electrons). In a simple approach, one can assume the electrons to be in a constant box potential within this system of conjugated double-bonds. One distinguishes linear systems (e.g. pinacyanol), circular systems (e.g. Cu-Phtalocyanin) and more complicated branched systems like in the case of rhodamine 6G. For linear molecules the eigenenergies of the n-th eigenstate then reads:

$$E_n = \frac{h^2 n^2}{8mL^2} \tag{2.1}$$

where h is Planck's constant, m is the electronic mass and L is the length of the box potential. For ring-like structures the same equation holds, however, there are two eigenstates to each eigenenergy (there are no fixed boundaries, resulting

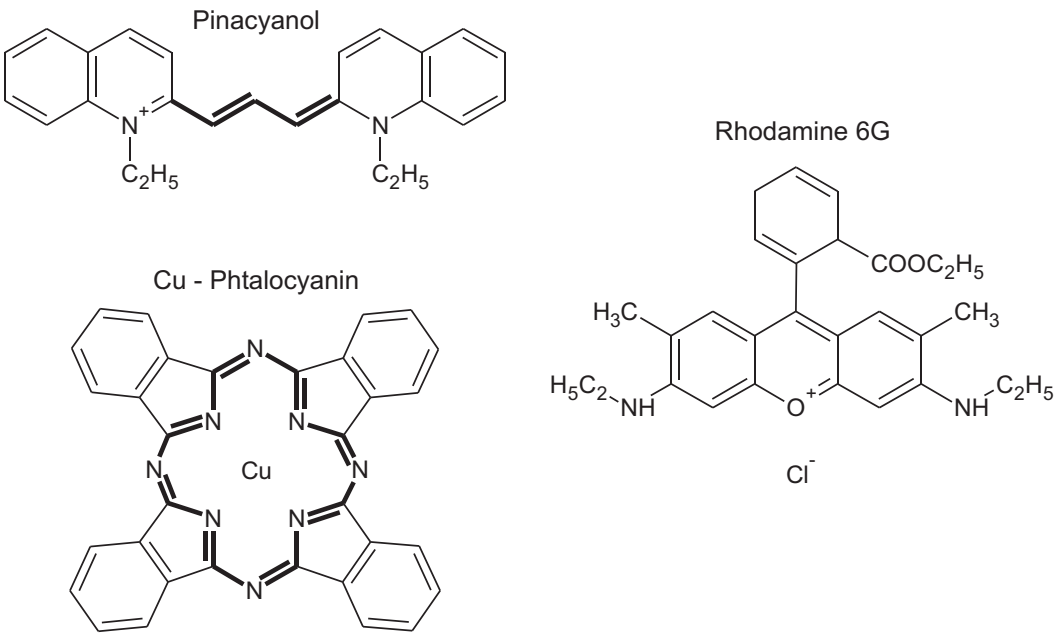

Figure 2.2: *Left:* Structure of two generic dyes with a linear and ring-like shape [51]; *Right:* Structure of hodamine 6G [54]

in distinct sine- and cosine-like solutions). Every state can now be occupied by two electrons. Thus, N π-electrons occupy the lowest $N/2$ states. The lowest absorption band arises from transitions from the $n = N/2$ to the $n = N/2 + 1$ state.

The corresponding energy difference and wavelength is:

$$E_{min} = \frac{h^2(N+1)}{8mL^2} \tag{2.2}$$

$$\lambda_{max} = \frac{8mc}{h}\frac{L^2}{N+1} \tag{2.3}$$

where c denotes the speed of light. In R6G rough estimations of the absorption wavelength are no longer that easy as it is neither linear, nor circular but there are several connected circles of π-electrons. However, for R6G-molecules the qualitative behavior described above still holds. In figure 2.2 one can find the chemical structure of R6G. Its absorption $\sigma_s(\lambda)$ and fluorescence $\Phi(\lambda)$ spectrum is depicted in figure 2.3. $\sigma_{em}(\lambda)$ is the cross-section for stimulated emission.

In a liquid solution large molecules experience in general more than 10^{12} collisions with solvent molecules per second. This means that the system reequilibrates

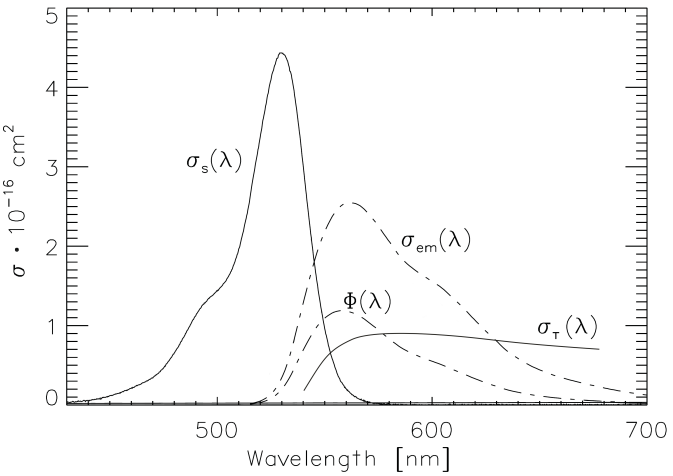

Figure 2.3: Fluorescence $\Phi(\lambda)$ and absorption $\sigma_s(\lambda)$ spectrum of a rhodamine 6G solution (10^{-3}mol^{-1}). The data is based on measurements of Fuh et al. 1998 [55]. Knowing the lifetime of the excited state, one can calculate the cross section for stimulated emission $\sigma_{em}(\lambda)$ (for more details: cf. [56]). An approximate curve for triplet state absorption $\sigma_T(\lambda)$ has been inserted.

on the order of picoseconds at room temperature ending up in the vibronic ground state of the first excited electronic state (or in any higher state according to Boltzmann's distribution).

The emission spectrum can now be obtained by mirroring the absorption spectrum around the frequency of the purely electronic transition. Absorption excites electrons from the electronic and vibrational ground state to any excited electronic and vibrational state, emission starts in the electronic excited state and vibrational ground state to any vibrational state of the electronic ground state (see figure 2.1).

Up to now, we did not take triplet states into account. For every electronic excited singlet state there is a corresponding triplet state. One can show with a simple argument that triplet state energies are inferior to the corresponding singlet state energies. The overall wave function for a system of two electrons in states m and n, at positions r_1, r_2 and with spins s_1, s_2 needs to fulfill Pauli's principle, i.e. the total wave function needs to be antisymmetric toward particle exchange. There are now two different possibilities: Either spins are parallel or antiparallel to each other leading to a symmetric or antisymmetric spin function. As a consequence, the corresponding wave functions needs to be antisymmetric or

symmetric, respectively.

$$\psi_s = \psi_{m,n}(r_1, r_2) + \psi_{n,m}(r_1, r_2) \qquad \text{symmetric wave function} \qquad (2.4)$$

$$\psi_{as} = \psi_{m,n}(r_1, r_2) - \psi_{n,m}(r_1, r_2) \qquad \text{antisymmetric wave function} \qquad (2.5)$$

Symmetry now leads to electrons being closer to each other than in the asymmetric case leading to a higher potential energy. Thus, triplet state energies are always lower than the corresponding singlet states and transitions occur, mediated by collisions with the solvent!

Figure 2.1 shows the relevant level scheme of rhodamine 6G. Optical pumping with green light (e.g. 515nm or 532nm) excites electrons from the S_0 ground state to a substate of S_1. By means of non-radiant processes (collisions with solvent molecules) electrons occupy the lowest S_1 state $\langle 3 \rangle$ - with $\langle 1 \rangle$, $\langle 2 \rangle$, $\langle 3 \rangle$ and $\langle 4 \rangle$ forming a four-level system.

There are several loss processes intrinsic to the gain medium. First of all spontaneous emission from $\langle 3 \rangle$ to $\langle 4 \rangle$ and collisions inducing transitions to T_1 depopulate the upper laser level. Moreover absorption of laser light to T_2 is actively damping the laser beam within the cavity.

Concluding, the most important principles of Dye Lasers are that to a good approximation the energy levels $\langle 2 \rangle$ are empty whereas $\langle 3 \rangle$ is populated by means of the pumping light. However, there are actually collision induced losses to the triplet state absorbing lasing light, thus, at a certain point higher pumping powers do not yield any higher output powers, but saturate. Furthermore, the dye liquid may heat up locally leading to instable laser operation. Both effects can be reduced using a dye jet, such that dye transferred to the triplet state is quickly removed out of the laser. As a rule of thumb the higher the speed of the jet the higher the pumping power can be chosen[4].

2.1.3 Singlemode Operation of Dye Lasers

In this section, the dye laser we use will be described. In figure 2.4 one can find a schematic overview of our ring dye laser manufactured by Radiant Dyes Laser & Accessories GmbH. All elements are mounted onto an invar bar for minimal thermal expansion of the cavity. Central feature is a polished nozzle of optical quality ejecting a thin film of dye solution (in the following referred to as dye jet) through the cavity into a catcher hose. The pressure needed is provided by a Radiant Dyes dye circulator pushing the dye solution through the dye nozzle at up to 7 bar.

[4]For our system saturation starts at about 7 W of pumping power for 6 bar of dye pressure. However, stable single-mode operation is only possible up to about 6 W.

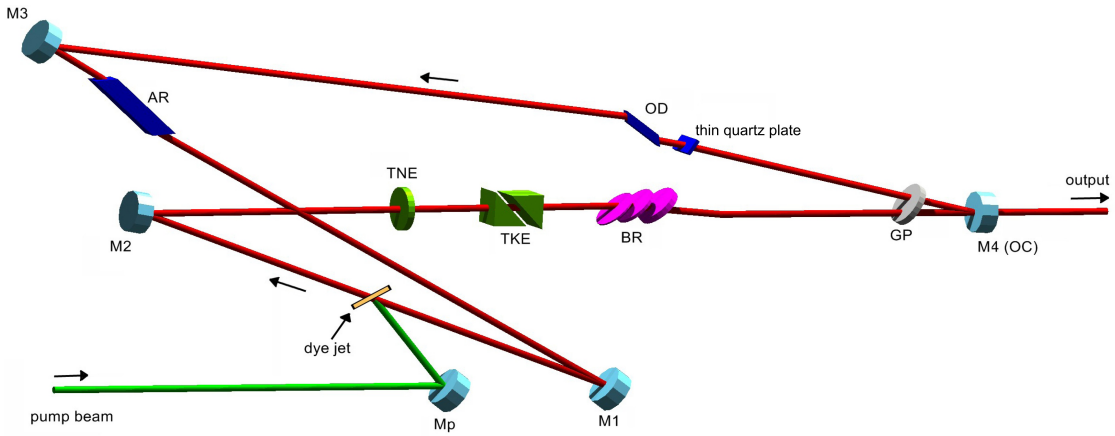

Figure 2.4: Overview on our ring dye laser, *source:* Manual for Radiant Dyes Ring Dye Laser

As a pump laser we use a Radiant Dyes MonoDisk[5] laser, which is a frequency doubled, diode pumped Yb:YAG ring laser emitting two laser beams of >10W each at 515 nm. This is due to the absence of an optical diode enabling two counter-propagating beams to persist. The active medium is inhomogeneously broadened permitting two different non-competing longitudinal modes.

One of the two outputs is focused onto the dye jet by Mirror Mp. Mirrors M1, M2, M3 and M4 are forming the cavity. M1 and M2 are concave mirrors with a radius of curvature $r = 150\,\text{mm}$ focusing the intracavity laser beam onto the dye jet.

2.1.3.1 Optical Diode (OD) and Thin Quartz Plate

In order to avoid competing counterpropagating beams an optical diode (also called Faraday isolator) is inserted into the cavity introducing additional losses for beams directed from M3 to M4. All optical elements made of glass (except for the etalons) are brought into the cavity under Brewster's angle. This induces losses for modes with polarization perpendicular to the laser plane. The quartz plate (i.e. $\lambda/2$-plate) rotates the polarization by 45°. Within the Faraday rotator (Faraday active crystal combined with a strong permanent magnet), the original polarization is restored for a beam traveling in the desired direction, but it is turned for a counterpropagating beam, which then suffers losses on subsequent circulations. As discussed in the previous section the mode with the highest gain per circulation will prevail - inhibiting counterpropagating beams.

[5] A modified ELS "MonoDisk" laser.

2.1.3.2 Selecting a Longitudinal Mode

Single-mode lasers that can be tuned close to an atomic resonance are a prerequisite for laser cooling. Their frequency accuracy needs to be smaller than the natural atomic linewidth, so for example 1 MHz in the case of sodium (line width $\Gamma = 2\pi \cdot 10\text{MHz}$). This corresponds to a relative frequency accuracy of about 10^{-9}. Simultaneously the tuning range of the gain medium (several tens of nanometers for R6G) should be conserved. It is intuitively clear that this is not feasible with only one optical element, as there has to be a tradeoff between the free spectral range (FSR, the frequency distance between two transmitted modes), the width of the transmission peak and the tunability. Instead several hierarchic filters are inserted, namely a birefringent filter, a thin and a thick etalon and, finally, the resonator itself that can be tuned by a tweeter and a galvo plate. These elements provide wavelength selectivity on scales of several nanometers (i.e. THz) to the order of MHZ in the order mentioned above. The product of the transmission profiles results in a sharply peaked curve permitting to suppress all but one mode. These elements will be described briefly in the following. Their assembly is sketched in figure 2.4.

2.1.3.3 Birefringent Filter (BR)

The birefringent filter is composed of a three-staged Lyot filter [57] with a thickness ratio between two subsequent filters of two.

The easiest case of a Lyot filter consists of a birefringent plano-parallel plate of thickness d (the optical axis lying inside the plane) followed by a polarizer. A laser beam hitting the surface perpendicularly, with a linear polarization angled 45° to the optical axis, may pass without any polarization changes if the condition

$$\|n_e - n_o\|\, d = N\lambda_N \tag{2.6}$$

or:

$$f(d, N) \stackrel{!}{=} \frac{Nc}{\|n_e - n_o\| d} \tag{2.7}$$

is fulfilled. Here N is an integer, n_e and n_o denote the extraordinary and ordinary refractive index respectively, thus, $\|n_e - n_o\|d$ is the difference between the optical path lengths within the crystal. If this difference is equal to a multiple of the wavelength $N\lambda_N$ no phase shift will happen. Light with a frequency satisfying equation (2.7), that has been derived using $f = c/\lambda_N$ (c: speed of light), passes the plate without any polarization changes.

Putting a polarizer behind the crystal transmitting the incident polarization, all frequencies given by equation (2.7) can pass through freely. The free spectral

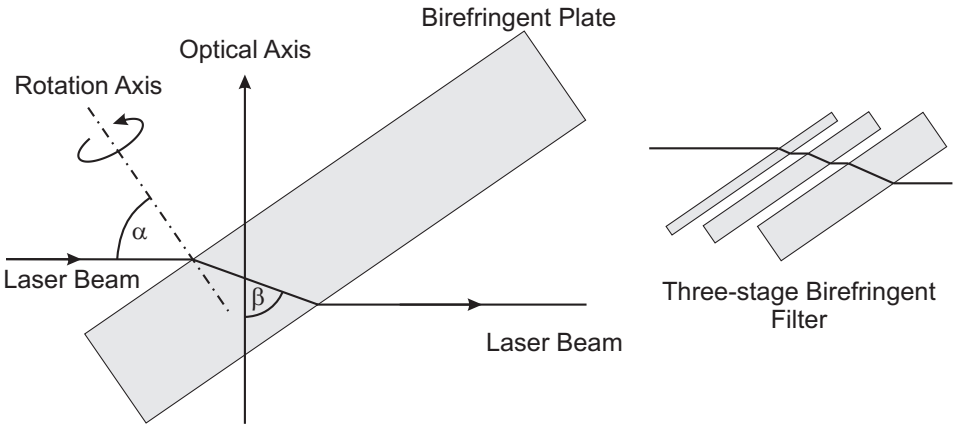

Figure 2.5: Schematic of a three-stage birefringent filter. On the *left* one of these stages is drawn.

range is given by

$$\Delta f(d) = \frac{c}{\|n_e - n_o\| d} \tag{2.8}$$

It is evident, that for all other wavelengths the outgoing polarization is elliptical or in special cases circular or linear, yielding losses between 0% and 100% at the polarizer. The overall transmission is given by [58]:

$$T(f, d) = \cos^2\left(\frac{\pi\,(f - f_0)}{\Delta f}\right) \tag{2.9}$$

where f_0 denotes some frequency with $T(f_0) = 1$ within the relevant frequency range. Concatenating several Lyot filters to the aforementioned three-staged birefringent filter results in narrower transmission peaks while conserving the free spectral range. See figure 2.6 for plots of single and combined transmission curves.

The assembly discussed so far does not allow for wavelength tuning. Furthermore, one can realize such a filter more easily in the case of a dye laser or any laser with a homogeneously broadened gain medium. As discussed in section 2.1.1 a very small percentage of additional losses is sufficient for the suppression of a mode in such a laser. Polarizers can be replaced by a plate under Brewster's angle. Refer to figure 2.5 for an overview. The plates are no longer perpendicular to the incident beam but are mounted rotatably and under Brewster's angle. Brewster surfaces serve as polarizers introducing this slight but sufficient loss on the perpendicularly polarized component. Another change is that the optical axis points out of the plane, thus, the angle between incident beam and optical axis varies while

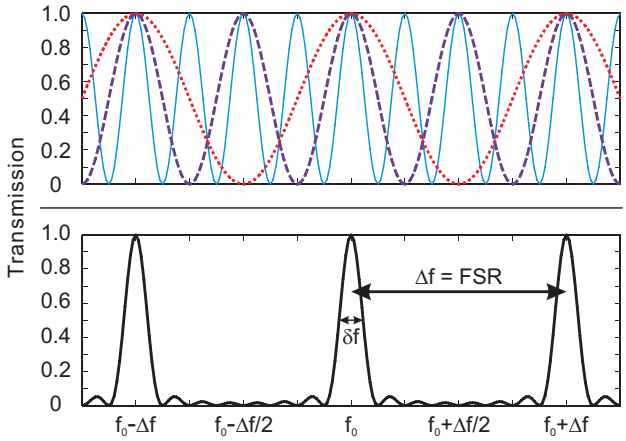

Figure 2.6: The upper figure shows transmission curves for Lyot filters with arbitrary thicknesses d (red, dotted line), 2d (violet, dashed line) and 4d (blue, solid line). Below the overall transmission of a subsequent arrangement of these three previous filters is shown. Δf is given by the free spectral range of the thinest plate $\Delta f(d_0)/2$, the FWHM is approximately equal to the FWHM of the thickest plate, i.e. $\sim \Delta f(4d_0)/2$

rotating the birefringent filter. As a consequence, $\|n_e - n_o\|$ can be changed and the transmitted wavelength can be tuned. However, an important disadvantage of a real birefringent filter is that one does not hit the ratio 2:1 perfectly well. As a consequence, maxima do not overlap automatically for all wavelengths specified in equation 2.7, but one has to rotate the Lyot filters slightly relative to each other in order to get this close to ideal overlap for the desired wavelength range. For a more detailed description refer to [58]. In our case the FSR is on the order of several tens of THz.

2.1.3.4 Thin and Thick Etalon (TNE and TKE)

The birefringent filter discussed above allows for tuning across the gain width of the dye, yet it is not sufficiently selective to achieve single mode operation. Now we would like to briefly present the function of the next levels in hierarchy, two Fabry-Perot etalons called thin and thick etalon.

The thin etalon is a 0.5 mm thick glass plate at close-to-normal incidence with coated surfaces for a reflectivity of about R=20%, yielding a FSR of about 200 GHz and a finesse[6] of $F = \frac{\pi}{2} \,/\, \arcsin\left(\frac{1-R}{2\sqrt{R}}\right) \sim 1.4$. It can be tuned by slightly rotating

[6]Ratio between free spectral range Δf and FWHM of the transmission peaks δf (nomencla-

its mount that incorporates a galvanometer simultaneously. This leads to a slight change of the optical path between the two surfaces and shifts the transmitted wavelengths.

The thick etalon is composed of two adjacent prisms (cf. figure 2.7) with a small distance between them, one of which is mounted onto a cylindrical piezo. Wavelength tuning can now be done by changing the voltage applied to the piezo. The inner surfaces are cut under Brewster's angle. The total thickness of the system is about 10 mm resulting in a FSR of about 10 GHz, also with a finesse of about 1.4.

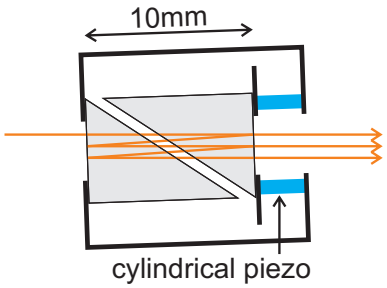

Figure 2.7: Schematic drawing of the thick etalon, refer to the text for details.

2.1.3.5 Tuning Resonator Modes: Galvo/Brewster Plate and Tweeter (GP and M2)

The mode spacing of the cavity is given by $\Delta f = c/l \approx 200\,\mathrm{MHz}$, where c denotes the speed of light and l the resonator length of about one and a half meters. When frequency sweeps are done this length needs to be adapted, since otherwise mode jumps between different cavity modes would appear. This feature is provided by the galvo plate (also called Brewster plate), a window brought into the resonator that can be turned by means of a galvanometer. Turning the GP leads to the desired changes of the resonator length as the optical path inside the plate (with refractive index of approx. 1.5) changes. The tuning range of the GP exceeds 30 GHz, however, the mechanical inertia inhibits fast changes and especially cannot compensate any fast fluctuations of the resonator length. This is where the tweeter (mirror M2 mounted onto a piezo) comes into play. It permits to change the resonator length quickly (on the order of kHz), but only with a small amplitude that corresponds to some hundreds of MHz.

ture like in 2.6). See any optics textbook for more details.

2.1.3.6 Locking the Laser to the Internal Fabry-Perot Cavity and Frequency Sweeps

Single mode operation at maximal output power is achieved, if all wavelength selective elements mentioned before are aligned such that their transmission maxima overlap in order to minimize losses for the desired wavelength and to get a maximal frequency selectivity (i.e. losses are substantially lower for exactly one longitudinal cavity mode than for all the others).

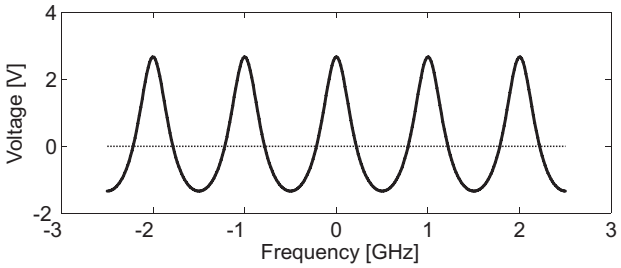

Figure 2.8: Transmission curve of the reference cavity registered by the photodiode, shifted to negative voltages such that locking can easily be done on any zero crossing of the signal.

How this overlap is realized in practice will be described in the following. First the birefringent filter is manually tuned to the approximate mode. One can clearly see mode hops of 200 GHz (FSR of the thin etalon) on a wavemeter while turning the micrometer-screw. Afterwards the thin etalon offset allows to select the right frequency to about 10 GHz, corresponding to the FSR of the thick etalon. The final position of the thin etalon is adjusted with a controller permitting to tune the center frequency of the thin etalon to $-15...+15$ GHz. The center wavelength to end up with is already now defined quite precisely. The remaining elements (TKE, GP, tweeter) are synchronized electronically. Therefore, about $2\times$ 1% of the outcoupled beam are split off. One is directed onto a photodiode directly (power signal), the other one passes through a temperature stabilized and tunable[7] Fabry-Perot cavity with FSR of about 1 GHz and a finesse of 2, and is captured by another photodiode. This signal (reference signal) is divided by the power signal compensating any intensity fluctuations.

The thick etalon locks one peak of the etalon transmission curve to the laser wavelength. This is realized using a lock-in technique: The thick etalon is modulated with a low amplitude at a frequency of approximately 2 kHz yielding a

[7] Inside the cavity there is another galvo plate that can shift transmission fringes by more than $\pm$15GHz

frequency modulation of its transmission curve and an amplitude modulation of the output power of the laser. The internal lock-in amplifier generates the error signal out of the power signal and feeds it back onto the TKE.

Galvo plate and tweeter are locked to the Reference cavity. Frequency locking is now done on any positive slope of the transmission spectrum. This is why the voltage level of the reference signal can be shifted to negative values (see figure 2.8 for a schematic). The zero-crossings define lock-points. It is now sufficient to take the registered and shifted signal as input for the control loops of galvo plate and tweeter.

Frequency scanning is simply achieved by scanning the reference cavity. A feed-forward signal is put onto the thin etalon that is followed by the TKE. Galvo plate and tweeter cancel any non-zero reference cavity signal and consequently follow the sweep.

2.2 Magneto-Optical Trapping

In this section, the concept of magneto-optical trapping will be introduced briefly. After a short introduction to light forces on two-level atoms we want to provide a basic understanding of how light forces can be used for cooling of neutral atoms. In the last part this concept will be extended to the case of multilevel atoms, where new effects like for example sub-Doppler cooling arise, always in view of the specific situation in a sample of sodium and lithium atoms. Finally, the working principle of a magneto-optical trap (MOT) will be described.

2.2.1 Light Forces on Two-Level Atoms

There are two distinct effects exerting forces on atoms. They are briefly described in the following. Note that only a classical motivation is given.

A quantum mechanical derivation can be found in the book of Metcalf and van der Straten [59]. The way to go is to establish a Hamiltonian containing a term coupling the eigenstates by means of a dipole operator to an electro-magnetical field. Diagonalization leads to the appearance of "new" eigenstates called dressed states. Inserting these states into a statistical density matrix approach and introducing spontaneous emission leads to the optical Bloch equations describing the time dependent behavior of these systems.

2.2.1.1 Dipole Force

Here, this aspect is only given for the sake of completeness. However, an important point for our future experiment will be the construction of an optical dipole trap [60, 61] precisely based on the optical dipole force[8]!

We would like to give a classical justification for this force. In a classical approach a two-level atom can be compared to a damped electrical resonator with the resonance frequency ω_0 and a dipole momentum of $\vec{p}$ driven by an inhomogeneous alternating electrical field $\vec{E}(\vec{x},t) = \vec{E_0}(\vec{x})\cos(\omega t)$. Solving the differential equation for a driven damped oscillator yield a phase difference between field and oscillator of:

$$\phi(\omega) = \arctan\left(\frac{2\beta\omega}{\omega_0^2 - \omega^2}\right) \tag{2.10}$$

where β is the damping coefficient. This equation is plotted in figure 2.9.

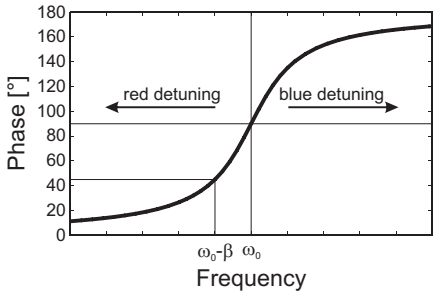

Figure 2.9: Relative phase between a driven oscillator and the driving field as a function of detuning

In electrodynamics the time averaged potential energy U of a dipole in an electric field is given by [62]:

$$U(\phi) = -\cos(\phi)\vec{p}\cdot\vec{E}(\vec{x}) \tag{2.11}$$

The qualitative behavior of U as a function of detuning can be deduced from figure 2.9. For blue detuning $-\cos(\phi)$ is positive, thus, the mean potential is increased whereas red detuning lowers the particle's potential energy. Finally, the $\vec{x}$-dependence of the electrical field induces a dipole force.

$$\vec{F}_{dip} = -\vec{\nabla}U(\phi) \tag{2.12}$$

Concluding, a dipole in an inhomogeneous alternating field is torn into the maximal field for red detuned ($\omega - \omega_0$ negative) light but seeks low fields for blue detuned

[8] Other names are reactive force, gradient force and redistribution force.

light ($\omega - \omega_0$ positive). For the conditions met in the aforementioned dipole trap a quantum mechanical calculation (dressed state approach) gives the following approximation:

$$\vec{F} = -\frac{\hbar\Gamma^2}{8\delta I_s}\vec{\nabla} I(\vec{x}) \tag{2.13}$$

where $I(\vec{x})$ denotes the laser beam intensity, I_s the saturation intensity of the transition and Γ the natural linewidth. δ is the laser detuning ($\delta = \omega - \omega_0$).

2.2.1.2 Light Pressure Force

Near and at resonance, also dissipative processes can be used for cooling. Whenever an atom absorbs light it gathers a photon's momentum $\vec{p}_{phot} = \hbar\vec{k}$. Once in the excited state there needs to be some kind of deexcitation through spontaneous or stimulated emission before a second excitation process can start. Consider now the two possible processes: Absorption followed by stimulated emission does not change the atom's momentum and will not serve for cooling since incoming and outgoing photons are the same. Spontaneous emission, on the other hand, leads to scattering of photons to random directions - thus, there is a mean net momentum of $N\vec{p}_{phot}$ acquired after scattering N photons. This force is called light pressure force[9] However, since electrons in the excited state have a non-zero lifetime $\tau = 1/\Gamma$ the rate of scattered photons is limited. It can be calculated using the following equation [59]:

$$\gamma_{scatter} = \frac{\Gamma}{2}\frac{S}{1 + S + \left(\frac{2\delta}{\Gamma}\right)^2} \tag{2.14}$$

$S = I/I_s$ is called saturation parameter with the transition and polarization specific saturation intensity I_s and δ denotes the detuning[10] of the laser relative to the resonance. In the limit of high saturation $\gamma_{scatter}$ approaches $\Gamma/2$. This corresponds to the situation that half of the atoms are in the excited state and spontaneous decays happen at a rate of Γ. Even though the recoil of the atom when absorbing one photon is only about 3 cm/s for sodium and lithium, the big linewidths of $\Gamma \approx 2\pi \cdot 10\,\mathrm{MHz}$ lead to accelerations on the order of $|a| = 10^5\,\mathrm{m/s^2}$!!

2.2.2 Optical Molasses

Up to now, we have neglected any effects arising from the movement of the atoms. Moving atoms experience a Doppler shifted light frequency and thus, a velocity

[9] This force is also known as scattering force, radiation pressure force and dissipative force.
[10] Containing the laser detuning but also Zeeman or Doppler shifts.

dependent detuning. In this case equation (2.14) needs to be modified slightly by redefining δ to be $\delta = \Delta + \vec{k} \cdot \vec{v}$, where Δ denotes the laser detuning and the second term corresponds to the Doppler shift. Given two red detuned laser beams in opposite directions, atoms moving in either direction are shifted into resonance with the counterpropagating beam and slowed down. Adding two more pairs of beams in the other spatial dimensions achieves efficient cooling. This setup is called optical molasses - the atoms behave like in a highly viscous fluid. Cooling to zero temperature is, of course, not achieved. On average, atoms are emitting photons of lower frequency than they are absorbing. The difference heats up the sample and cancels the cooling effect at some point. The corresponding temperature is referred to as "Doppler temperature".

This cooling scheme is called Doppler cooling and yields temperatures on the order of hundreds of μK [63].

2.2.3 Magneto-Optical Trapping of Multilevel Atoms

There are several changes when switching to real atoms. First of all there are evidently more relevant and accessible energy levels, like can be found in the simplified level scheme of sodium in figure 2.10 where F denotes the total angular momentum including the electron's and core's spin and the angular momentum of the electrons. Each of the F states is now composed of 2F+1 degenerate magnetic substates[11] as shown in figure 2.10 for two energy levels.

Even though all this looks quite differently from what has been discussed, the cooling mechanism described above still works – even better (see 2.2.4). The laser is tuned slightly below the resonance F=2 to F'=3 and pairs of σ^+ and σ^- polarized[12] counterpropagating beams are used. This drives the atoms to either of the outermost substates shown in figure 2.10, depending on the direction the atom is moving in and results in a Doppler cooling scheme.

Up to now, atoms may be cold, but trapping is not yet achieved since no position dependent force is established. Inserting two magnetic coils in an anti-Helmholtz configuration yields a magnetic quadrupole field. The magnetic field introduces a position dependent Zeeman shift of the magnetic sublevels. The resonance frequency of the cycling transition is shifted by

$$\Delta_{Zeeman} = \frac{1}{\hbar}\left(g_{m'_F} - g_{m_F}\right)\mu_B B(\vec{x}) \approx 1.4\,\mathrm{MHz/G} \cdot B(\vec{x}) \tag{2.15}$$

[11] For an introduction to selection rules and designation of levels in atoms refer to any standard textbook like [50].

[12] Often both of the beams are attributed the same polarization, however, this is a question of the reference frame.

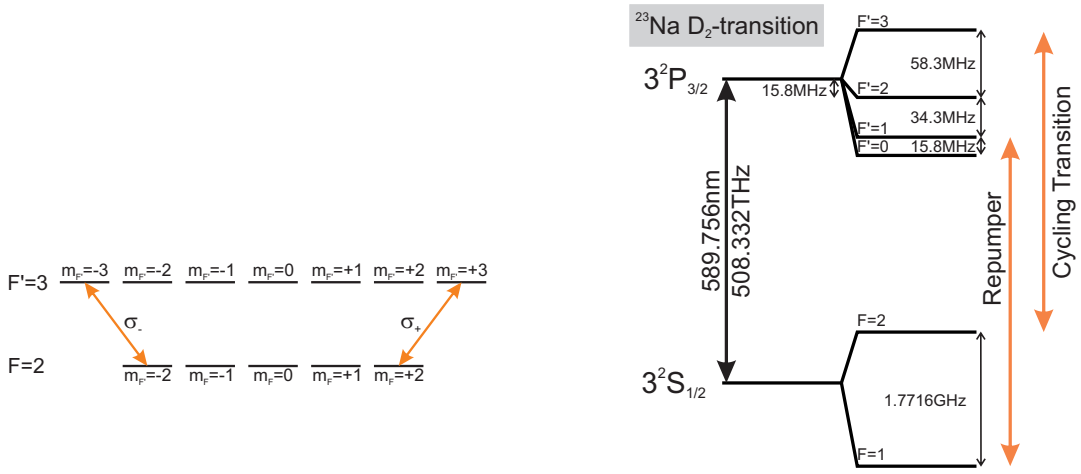

(a) (b)

Figure 2.10: *a)*: Magnetic substates of the cycling transition used for sodium, *b)*: Level scheme of sodium.

where g_{m_F} and $g_{m'_F}$ are the Landé factors of the involved states (see figure 2.11) [64, 65]. This equation holds only for low magnetic fields as long as the nuclear spin is mainly coupled to the spin-orbit momentum of the valence electron (compared to the coupling to the external magnetic field). We now have to modify equation (2.14) a last time including equation 2.15. Now the scattering rate, finally, reads:

$$\gamma_{scatter} = \frac{\Gamma}{2} \frac{S}{1 + S + \left(\frac{2(\Delta + \vec{k}\cdot\vec{v} + \Delta_{Zeeman})}{\Gamma}\right)^2}$$

A schematic of the line shifts is given in figure 2.11. Choosing the right magnetic field direction implies a force always directed to the magnetic zero.

In conclusion, there are two effects leading to magneto-optical trapping. Whenever an atom has got a certain velocity its absorption line is shifted into resonance with a beam traveling in opposite direction. Whenever an atom is off the center of the magnetic quadrupole field the cycling transition is shifted into resonance with a counterpropagating beam, leading to a backward force. This is visualized in figure 2.11. The motion of atoms in a MOT is now characterized by a spring constant attributed to the Zeeman shifting and a damping coefficient arising from the optical molasses. Since damping is much bigger than the spring constant, the atomic motion is overdamped.

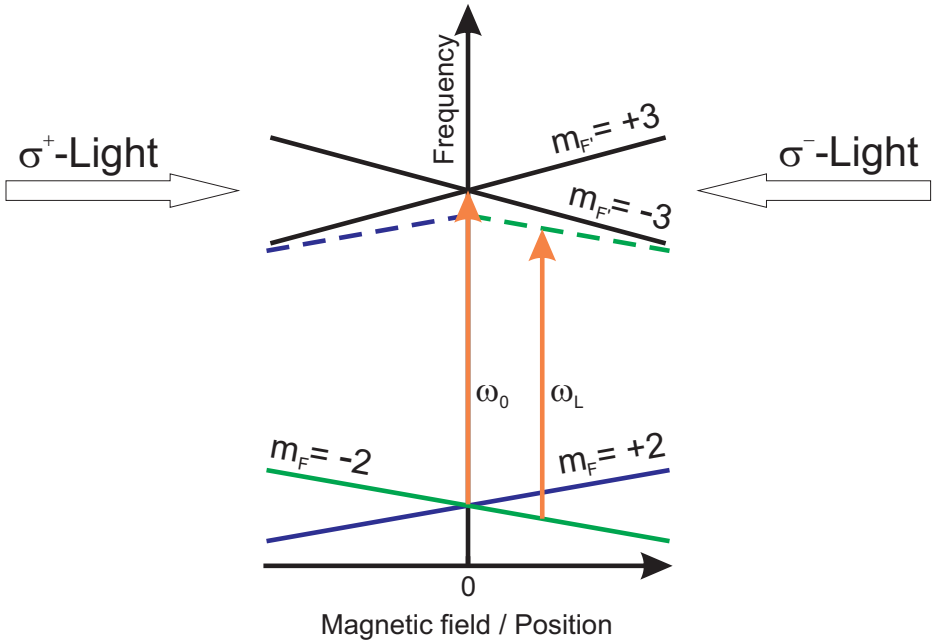

Figure 2.11: Trapping schematic in a MOT. σ^+ and σ^- denote the polarization of the light beams coming from the left and right respectively. ω_0 denotes the unshifted resonance frequency, ω_L is the frequency of the laser beams that is slightly detuned to the red. Read the x-axis to be the magnetic field or in the case of a MOT with $B(x) \propto x$ also as the position in a trap. For weak magnetic fields the Zeeman substates are shifted such that $\Delta_{Zeeman} = \frac{1}{\hbar}(g_{F'}m_{F'} - g_F m_F)\mu_B B(\vec{x})$, with $F' = 3$, $F = 2$, $m_{F'} = \pm 3$, $m_F = \pm 2$, $g_{F'} = 0.6671$ and $g_F = 0.5006 \rightarrow g_{F'}m_{F'} - g_F m_F = \pm 1.0002 \approx \pm 1$ [64]. An atom on the right will mainly absorb photons from the σ^--beam and vice versa, pushing the atoms to the center.

2.2.4 Sub-Doppler Cooling

The standing light wave, formed by two counter-propagating, circularly polarized beams, is linearly polarized at each point. The polarization vector rotates along the beam with a periodicity of half the wavelength. This influences transition amplitudes within the level scheme in such a way that an additional cooling mechanism arises leading to more efficient cooling, referred to as sub-Doppler cooling [66, 67]. Temperatures on the order of 10μK can be achieved for sodium, corresponding to the kinetic energy associated with a single photon momentum recoil. This is referred to as the recoil limit.

Already at that point it becomes clear that sub-Doppler cooling will not work for lithium (see figure 3.4). The excited states are separated by less than the

natural linewidth, thus, selective excitation of only one F state is not feasible.

2.2.5 Repumping

One point has not been mentioned yet. According to equation (2.14) electrons in sodium may also be excited to the F'=2 state, since the level spacing is not infinite. Thus, transitions to the F=1 state are no longer dipole forbidden. Once an atom is in the F=1 state it is no longer trapped and needs to be transferred back to the F=2 state. Therefore, a repumping beam resonant with the F=1 to F'=2 or F'=1 transition is added. This effect is even more pronounced in lithium due to the quasi-degeneracy of the excited states. See 3.5.2 for more details.

2.2.6 Limitations and the Dark Spot MOT for Sodium

The density in a sodium MOT is limited to about $10^{11}\,\mathrm{cm}^{-3}$ mainly by a process called radiation trapping [68]. Already at much lower densities the atoms are no longer interacting only with the light field but they also reabsorb photons that have been scattered by the others. These incoherent processes introduce a repulsive force between the atoms and keep them apart.

This peak density can be increased by nearly a factor of ten if the atoms in the center of the trap are in the untrapped F=1 ground state. This can be achieved by removing the repumping light in the center of the trap ("dark spot")[13] [69]. Without a repumping beam the atoms fall down to the dark F=1 state after about 100 scattering processes and radiation trapping is reduced. Repumping only occurs at the edge of the MOT, keeping the atoms in the middle.

[13] Originally SPOT is a short form for SPontaneous-force Optical Trap.

3 Experimental Setup

The following chapter will give an overview of our setup with an emphasis on the laser system. We use two optical tables of $3\,\mathrm{m} \times 1.5\,\mathrm{m}$ each for the vacuum setup on the one hand and for all the optics and light preparation on the other hand. The two are interconnected using optical fibers for the light and a BNC bus for the exchange of data.

3.1 Introduction

In figure 3.1 we show an overview of our vacuum system that has been set up during the last year. As it is characterized in more detail in Marc Repp's diploma thesis we will only give a short summary on design guidelines and functionalities in the following. The objective of our apparatus is to cool as many ^{6}Li atoms as possible - on the order of 10^7 should be realistic [70] - to the lowest temperatures in reasonably short time. Limiting factor for the number of fermions in the degenerate phase is the number of sodium atoms initially trapped, since sympathetic cooling results in huge losses of sodium atoms. The group of W. Ketterle reports on losses of about 50% for lithium during the transfer to the magnetic trap and another factor of two during the sympathetic cooling stage [71]. Thus, a lithium atom number on the order of 10^8 in the MOT should be sufficient.

These 10^7 ^{6}Li -atoms need to be cooled at the expense of sodium. So cooling will only be possible as long as sufficiently many sodium atoms are available. Taking into account transfer efficiencies from the MOT to the magnetic trap of about 30% for sodium[1], less than 1% of the sodium atoms are left after evaporative cooling, where this number highly depends on the starting and final temperature as well as the atom number in the fermionic cloud. As a rule of thumb sympathetic cooling is efficient as long as there is at least a comparable number of sodium in

[1] Up to ≈70% can be achieved with more elaborate transfer mechanisms to the $|\mathrm{F'}, \mathrm{m_{F'}}\rangle = |1, -1\rangle$ state [48]. However, these are not applicable in our case. See discussion in [71] and in section 3.4.2.

the magnetic trap [71]. Thus, an initial 10^{10} sodium atoms should be captured in the MOT.

3.2 Vacuum System

For this experiment a vacuum apparatus with a residual pressure well below 10^{-10} mbar is needed. This is for several reasons. The mean free path of the atoms needs to be much larger than the length of the apparatus, such that the atoms in the atomic beam are not deflected on their way from the oven to the glass cell (see next section). However, the stronger constraint is, that during an experiment, i.e. on the order of a minute, cold atoms should not collide with hot atoms.

3.2.1 The Vacuum Chamber

A possible way to high loading rates using sodium and lithium is a linear setup with ovens, a Zeeman slower and a glass cell.

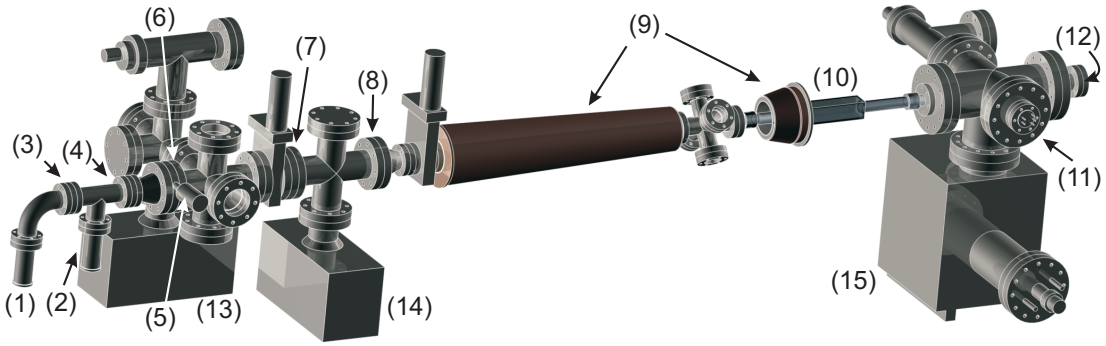

Figure 3.1: Overview of our vacuum apparatus, see text for more details.

In the following the numbering relates to figure 3.1. Our setup consists of an arrangement of two ovens for sodium (1) and lithium (2), heated up to 270 °C and 350 °C respectively. They are connected through an angled mixing nozzle (3) that allows liquid sodium to flow back into the reservoir. These temperatures are needed in order to increase the (very low) vapor pressures for these two elements (cf. [64, 65]). Sodium and lithium vapors are brought together in the lithium part of the oven and finally diffuse into the apparatus through a conical hole with inner diameter of 4 mm (referred to as "oven nozzle") (4). Pressures and, thus, the ratio of emitted atoms into the ultra high vacuum chamber and the total flux

can be adjusted by selecting the temperatures in the two oven chambers. About 10 cm behind the oven nozzle there is a rotary feedthrough (5) inserted into our vacuum system. This feedthrough is connected to a thin plate made of stainless steel serving as a shutter for the atomic beam. During this diploma thesis a driver has been developed, that allows to switch the atomic beam on and off with TTL signals. Basically this driver uses a standard RC-servo and is controlled by a small PIC microcontroller. See appendix B for more details.

A small aperture at position (6) is blocking atoms on off-axis trajectories. The transmitted atomic beam is sent through two differential pumping tubes ((7) and (8)) permitting to decrease the residual gas pressure gradually from $5 \cdot 10^{-8}$ mbar to 10^{-11} mbar. We will present the Zeeman slower (9) in the next section. The Zeeman slower is put as close as possible to the glass cell avoiding too many losses due to the elevated divergence of the beam at that point. The glass cell (10) itself is attached to flexible bellow adapters via a glass to metal transition[2]. Behind the glass cell, there is a vacuum gauge (11) and a window for the Zeeman slower beam (12).

3.2.2 Pumping

Our vacuum setup is evacuated by two 55 l/s ion getter pumps (one (13) in the oven and collimation section, the other one (14) in between the two differential pumping tubes) and a 150 l/s ion getter pump (15) combined with a titanium sublimation pump (about 1000 l/s) behind the glass cell.

For a more detailed description of our setup and an analysis of vacuum conductivities and pumping speeds refer to Marc Repp's diploma thesis [72].

3.3 Zeeman Slower

A Zeeman slower has been installed in order to increase the flux of slow capturable atoms in the glass cell. Loading of a magneto-optical trap requires slow atoms with speeds of less than 30 m/s as a rough estimate, whereas the velocity distribution of sodium and lithium atoms is centered around 800 m/s and 1600 m/s for the given oven temperatures. Evidently, only a very small fraction is captured without further precautions. In the Zeeman slower atoms can be decelerated to the required speed. Our slower is designed such that sodium and lithium atoms with initial

[2] When heating up the vacuum the different specific expansion coefficients of steel and glass would in either case make the cell burst. So the expansion coefficient needs to be changed gradually.

speeds of up to 700 m/s can be slowed down. The most probable velocity of the atoms leaving the oven is about the same for sodium, but about twice as high for lithium. Thus, the ratio of slowed sodium atoms is much bigger than that of lithium. Since more sodium than lithium is needed for the further cooling, this is not a restricting point.

Below I will briefly describe the functional principle of a Zeeman slower and some design criteria of the one we set up. For more details on any point refer to Jan Krieger's diploma thesis [73].

3.3.1 Design Criteria

- Our slower was designed for sodium. As discussed before, more sodium than lithium is needed for further cooling steps. A sodium slower always works for lithium but is more conservative[3].

- The slower should be considerably shorter than 1 m, first for keeping the apparatus compact, but also since the (geometric) divergence of the atomic beam cancels the slowing effect at some point. Random scattering of the absorbed photons leads to additional transversal heating, i.e. divergence.

- In order to compensate for imperfections of the magnetic field the design used a saturation parameter S equal to one, even though more laser power is available.

- The magnetic field should not be excessively high close to the center of the MOT coils, since it has to vanish there. In addition, the Zeeman slower beam should not be resonant to the atoms in the MOT. This condition requires a non-zero field at the end of the slower.

3.3.2 The Setup and a Basic Introduction

Our Zeeman slower consists of two solenoids with an overall length of about 70 cm with an additional free space of about 20 cm between them. The solenoids are concentric to the atomic beam. Along this axis a laser beam and the atomic beam counterpropagate. Whenever the circularly polarized laser beam is resonant with an electronic transition light is absorbed and scattered into any direction, leading to a mean deceleration. Shaping the magnetic field $B(z)$ such that deceleration (i.e. Doppler shift of the atomic lines) is compensated by Zeeman shifts of the used

[3] A slower designed for lithium only would have been shorter while maintaining the same slowed fraction of slowed atoms.

transitions the atoms are resonant all along the magnetic field and, thus, slowed down.

Atoms moving at velocity v in a position dependent magnetic field $B(z)$ with a counterpropagating laser beam with wavenumber k experience a deceleration

$$a(z,v) = \frac{\hbar k}{m}\frac{\Gamma}{2}\frac{S}{1+S+\left(\frac{2\delta(z,v)}{\Gamma}\right)^2} \tag{3.1}$$

$$\delta(z,v) = \delta_0 + \vec{k}\cdot\vec{v} - \frac{\mu_B g B(z)}{\hbar} \tag{3.2}$$

where $\hbar$ denotes the reduced Planck constant, Γ is the line width of the transition of the excited atoms, the Landé factor g for the used transition is very close to one [64, 65], m is the atomic mass and S is the saturation parameter (refer to [59] for more details on atom light interaction). δ_0 is called laser detuning and is given by the difference between the laser and the atomic resonance frequency. Elimination of v while keeping a constant for all z implies a square-root shaped magnetic field. Main characteristics of a Zeeman slower are the S parameter needed for slowing (in our case S should be on the order of 1), the maximal velocity that can be slowed (in our case about 700 m/s for both species) and the configuration of the magnetic fields. We set up a slower in a so-called zero crossing configuration (also known as "spin-flip slower" [74]). "Increasing field" and "decreasing field" slowers do not need a zero-crossing. However, they have their maximal magnetic field close to the MOT or zero field close to the MOT, i.e. Zeeman slower light is resonant with the atoms in the MOT.

This means that the magnetic field starts at about 600 G and decreases down to −200 G. In the zero field domain atoms have to repolarize because of the change in magnetic field direction leading to a change from σ^+ to σ^- light in the rest frame of the atoms. The advantage of such a configuration is that the magnetic field close to the magneto-optical trap is relatively small (about 200 G). So compensation of the magnetic field can be achieved with little effort. This is necessary, since the magneto-optical and magnetic trap would be perturbed. On the other hand, the Zeeman laser beam is still far detuned relative to the unshifted resonance and MOT operation is not disturbed by this light. The only disadvantage is that one needs repumping light since during the repolarization at zero field any magnetic substate of the excited state is populated. So decays to the ground state $3^2S_{1/2}$, F=1 may occur, and atoms in that "dark state" would be lost for further slowing. Another point is that sufficient time for this repolarization process needs to be provided resulting in a longer slower.

3.4 Magnetic Fields

For magneto-optical trapping, magnetic trapping and tuning of scattering lengths in the vicinity of Feshbach resonances only one single pair of coils are used, creating a quadrupole field in an anti-Helmholtz configuration or a homogeneous field at the center for a Helmholtz configuration, depending on the relative polarity of the coils. Here the Feshbach coils are the challenging part. They will be described in the following.

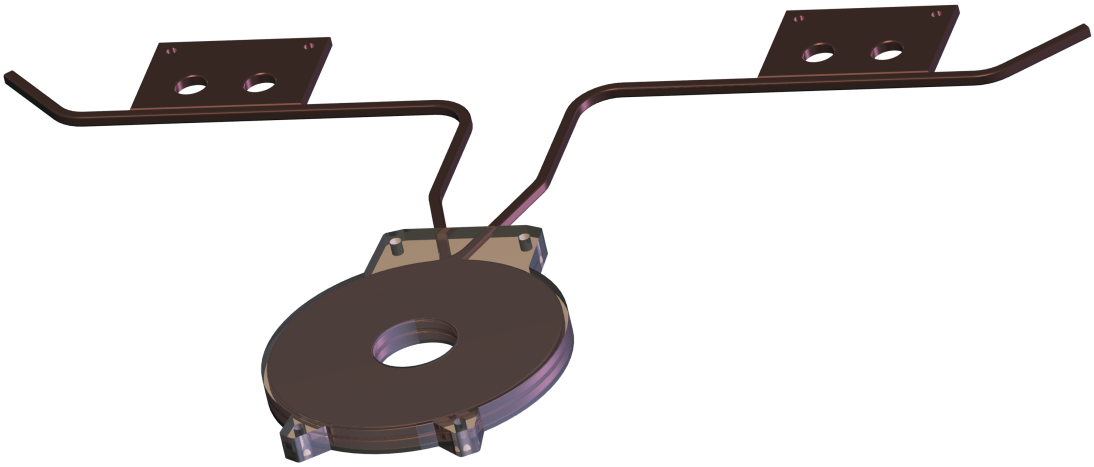

Figure 3.2: Drawing of our multi functional coils used for magneto-optical and magnetic trapping as well as for Feshbach fields

3.4.1 Feshbach Coils

Tuning over atomic Feshbach resonances of a degenerate Fermi gas opens up a wide field of exciting physics that becomes accessible as described in the introduction (see chapter 1.2). In a standard experiment interaction is tuned to some scattering length in the range of the Feshbach resonance, i.e. a magnetic field of about 830 G for ^{6}Li . Typically, the interaction needs to be switched very quickly. Our coils are designed such that they can be switched from 1000 G to zero in less than 20 μs. For a minimal switching time and bearable inductive voltages the inductance needs to be kept as low as possible. So in order to reach the high magnetic fields huge currents (up to 440 A in our case) have to be put through the wire leading to dissipated powers on the order of 2 kW. Heat management is an important point since any temperature instability causes fluctuations of the magnetic field gradient.

In this kind of experiment one relies on reproducible results on a timescale of hours, thus, any heating effects have to be minimized. The assembly that is currently set up consists of four coils of the type shown in figure 3.2, two above and two below the glass cell with 15 windings each. Hollow squared wire has been used such that the heat can be removed by temperature-regulated water flowing through. The assembly is embedded in epoxy.

3.4.2 Magnetic Trap

For magnetic trapping we will use a quadrupole magnetic field. Therefore, the multi function coils are switched to an anti-Helmholtz configuration by means of a bridge circuit based on insulated-gate bipolar transistors (IGBT[4]) (for more details refer to the diploma thesis of Anton Piccardo-Selg [75]). The magnetic field is zero in the center of the assembly and increases linearly in radial and axial direction (with a gradient that is twice the value for the radial direction). For magnetic trapping the atoms need to be transferred to some low-field seeking state that is immune towards spin-exchange collisions[5]. These atoms will now oscillate around the zero.

There are only two states for sodium with a non-vanishing magnetic moment satisfying these conditions, namely $|\mathrm{F},\ \mathrm{m_F}\rangle = |1,\ -1\rangle$ and $|2,\ 2\rangle$. The $|1,\ -1\rangle$ state is preferred[6] by far for creating sodium BECs, yet it undergoes spin exchange collisions with lithium (see discussion in [71, 48]). So the $|2,\ 2\rangle$ state is the one to choose. Optical pumping in a small magnetical bias field allows to transfer the atoms to the $|2,\ 2\rangle$ state (see section 3.5.2.7).

Once in the center there is no longer a polarizing field, spin flips occur and atoms (in untrapped states) are lost. In order to avoid this, several trap configurations have been developed such as clover-leaf [77], Ioffe-Pritchard [78] or time-orbiting potential (TOP) [79] traps. We use a standard quadrupole magnetic field combined with a blue detuned laser beam[7] focused into the center of the trap ("optical plug", [80]). The light shift potential[8] induced by this beam keeps the trapped atoms away from the magnetic zero.

[4] Transistors designed for switching of high currents, i.e. several hundreds of Ampères.

[5] Collisions that change the internal spin state of the atoms, transferring them from a trapped to an untrapped state

[6] Not only the $|2,\ 2\rangle$ state, but also the $|2,\ 1\rangle$ and $|2,\ 0\rangle$ are (at least weakly) trappable in a the magnetic trap. Since there are spin exchange collisions between them, the latter need to be completely removed in order to close this loss channel [71, 48, 76].

[7] We will use some of the pump laser power at 515 nm.

[8] Potential attributed to the optical dipole force of the light (see 2.2.1.1).

3.5 The Laser System

As described in section 2.1.3 our laser system is based on two Radiant Dyes Ring Dye Lasers. They are pumped by a frequency doubled Yb:YAG disc laser with two outputs at >10 W each. For sodium we are using a dye solution of rhodamine 6G in ethylene glycol. The concentration is set such that the pump laser beam is absorbed to about 98% within the dye jet yielding concentrations of about 0.8 g/l. The maximal power exceeds 1 W for 8 W of pumping power. However, stable, mode-hop free operation is currently only possible at about 800 mW. This is probably due to heating of the dye in the center of the pumping spot. With a higher dye jet speed higher stable powers should be easily achievable. Therefore, either more powerful dye circulators, or a thicker dye nozzle are needed. The dye used for Lithium light is DCM with a concentration of about 0.8 g/l in a mixture of 50% ethylene glycol, 18% benzyl alcohol and 32% propylene carbonate. Its power exceeds 1.5 W. Stability tests have not yet been performed.

3.5.1 Why Dye Lasers?

Because there is currently no well-developed alternative for sodium light at 589nm.

At the Laboratoire Kastler-Brossel (ENS) Fabrice Gerbier *et al.* are currently developing a solid state laser at 589 nm using frequency mixing of diode lasers. However, power output is below 400 mW up to now. Already available commercially are small Diode Pumped Solid State (DPSS) modules with a second harmonic generator but they are far away from single mode.

In the case of lithium there are actually cheap laser diodes with powers of up to 100 mW available (e.g. laser diode type HL6545MG[9]) that are used in DVD recorders. Another alternative would have been Toptica's TA modules (based on tapered amplifiers) offering up to 500 mW. But even though dye lasers are more demanding than solid state lasers they offer a mode quality that is far better than laser diodes. Additionally the output power is sufficiently high.

3.5.2 Frequencies

All frequencies had to be derived from one single laser using acousto-optical (AOM) and electro-optical (EOM) modulators. Consequently, the design of the laser system has to comply with some basic requirements:

[9]These diodes have rated powers of up to 120 mW. However, their typical wavelength is 662 nm and they need to be heated up to about 65°C for 671 nm.

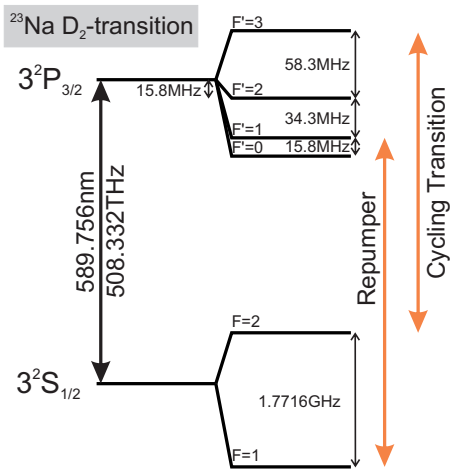

Figure 3.3: Level scheme of ^{23}Na

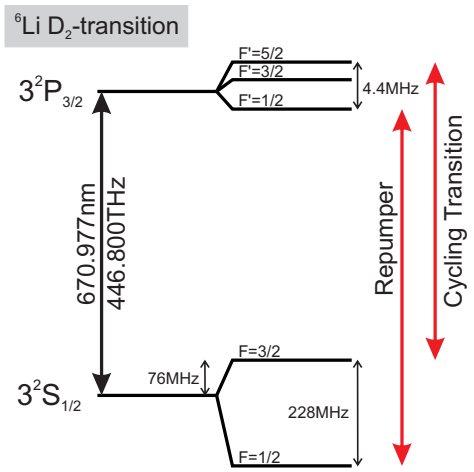

Figure 3.4: Level scheme of ^{6}Li

- efficient use of laser power
- maximal tunability of frequencies
- cost effective use of standard optics (thus, especially use of standard AOMs)

Figures 3.3 and 3.4 show the level schemes of the relevant transitions in ^{23}Na and ^{6}Li. For simplicity the D_1-lines have been omitted. They are about 400 GHz and 10 GHz below the corresponding D_2-lines for sodium and lithium and, thus, not interfering with any process discussed in the following.

In the following we will give an overview of the frequencies needed. The lithium laser system has not been set up until now, so only a proposed scheme is given in figure 3.9 and table 3.1.

3.5.2.1 Locking the Laser to an Atomic Resonance

Both lasers are locked internally to a temperature stabilized reference cavity with a short term stability of about 1MHz. However, on the timescale of hours (or even seconds) a stability well below the natural linewidth of lithium ($\Gamma_{Li} = 2\pi \cdot 6\,\mathrm{MHz}$) and sodium ($\Gamma_{Na} = 2\pi \cdot 10\,\mathrm{MHz}$) can not be guaranteed[10]. Long-term stability is provided by locking the laser to an atomic transition. At room temperature, a cell filled with some ^{23}Na or ^{6}Li is not sufficient to show appreciable absorption due to

[10]The time constant of the feedback loop is limited by the mechanical (!) galvo plate within the reference cavity, thus, on the order of hundredths of seconds.

the minuscule vapor pressure of both species. Therefore, absorption cells have to be heated up to about 130°C and 240°C, respectively. A sodium spectroscopy oven has been set up during this diploma thesis, based on an evacuated glass cell filled with sodium. More technical details on this and on Doppler-free spectroscopy can be found in appendix D. For lithium, a somewhat more elaborate scheme is needed because lithium diffuses into glass and chemically reacts with it. This leads to an increased opacity and permanent damage. Typically, this problem is overcome using a so-called heatpipe, a relatively long and thin tube made of high-grade steel, that is heated in the middle. The inner surface is covered with a high-grade steel mesh. The windows attached on either side are kept at room temperature and a small amount of buffer gas is brought into it, avoiding any direct collisions with the windows. Lithium atoms hitting the walls off the center stick to them and diffuse back to the center along the mesh. See [16, 81] for a more detailed analysis and concrete implementations.

The sodium laser is locked to a frequency of **-180MHz**[11] relative to the cycling transition, mainly because this simplifies the whole optics scheme. Another point about this is, that any stray light is far detuned (about 8Γ) relative to the next atomic resonances, thus, not interfering at any point. The laser is not locked directly to the F=2 to F'=3 transition but to the most significant feature of the spectrum, i.e. the cross-over of the transitions F=2 to F'=3 / F'=2, that is about **-29MHz** red detuned. Therefore, one needs to shift up the laser's frequency by about ***+151MHz*** before doing spectroscopy. A measured spectrum can be found in figures D.5 and D.6.

3.5.2.2 MOT

For magneto-optical trapping light is usually detuned by several linewidths. For sodium atoms, however, a red detuned beam is at the same time blue detuned for the F=2 to F'=2 transition and, thus, pushes out the atoms. This influence can only be reduced by choosing a relatively small detuning. Up to now, we are using **-15MHz** ***(+165MHz)*** as a compromise of the values used in the groups of W. Ketterle (∼**-20MHz**) and P. van der Straten (∼**-11MHz**), since no systematics have been done yet[12].

[11] any **bold** frequencies given are from here on meant to be relative to the cycling transition, ***bold italic*** frequencies relative to the laser frequency

[12] One might think of choosing a MOT frequency below the lowest hyper-fine state at <**110MHz**, however, in this case only Doppler cooling will occur. At the same time, repumping power needs to be increased drastically since transitions to the F=1 state are no longer forbidden – an inconvenient point as will be seen in the next section

	^{23}Na			^{6}Li	
	δ MHz	δ_{rel} MHz	Intensity	δ MHz	δ_{rel} MHz
MOT	−15	+165	$> I_{sat}$	−25	+157
MOT repumper	+1679	+1859	4 mW	+228	+410
Zeeman slower	−350	−170	$I_Z \gg I_{sat}$	−344	−162
Zeeman slower repumper	+1713	o[13]	$\approx 10\% \cdot I_Z$	−116	+66
Imaging	0	+180	< 1 mW	0	+182
Transfer	−58	+122	$\approx I_{sat}$	o[14]	
Lock Frequency	−180	0	0.5 mW	−182	0

Table 3.1: Frequencies needed, where δ is the detuning relative to the atomic resonance and δ_{rel} is the detuning relative to the laser frequency.

3.5.2.3 MOT Repumper

A priori the cycling transition in sodium is closed, where closed means, that decays into the "wrong" F=1 ground state are dipole forbidden. Since the hyper-fine splitting of the excited state is small compared to the linewidth, excitations to the F'=2 state actually may occur. Electrons may now decay into the F=1 state and are no longer trapped. Putting a repumping beam resonant with the F=1 to F'=1 (**+1679** - ***+1859***) transition returns atoms into the cycle. Taking the relevant Clebsch-Gordan coefficients into account the F=1 to F'=2 transition would have been favorable. The advantage of our selected resonance is that, given a repumping beam that counterpropagates the Zeeman slowed atomic beam under an angle of about 50°, the atoms experience shifted light, that is resonant with the F=1 to F'=2 transition. In conclusion the F=1 to F'=1 transition is used for repumping of trapped atoms, the F=1 to F'=2 transition for the incident beam that is about to be trapped. Yet the effect of this method still has to be evaluated.

3.5.2.4 Zeeman Slower

The magnetic end field and the desired speed of the atoms define the detuning for the Zeeman slowing beam. We arbitrarily chose the magnetic field maximum close to the glass cell to be 214 G with a speed of the atoms of $v_{end} = 30$ m/s, corresponding to the capture velocity of the MOT. The contribution for the relevant Zeeman shift and Doppler shift reads now:

[13] Sidebands are directly modulated onto the Zeeman slower beam.
[14] Hyper-fine levels of excited state are not resolved.

$$\Delta_{Zeeman,\,end} = -\mu_B B_{end} = -1.4\text{MHz/G} \cdot 214\text{G} = 300\text{MHz} \tag{3.3}$$
$$\Delta_{Doppler,\,end} = -v_{end}/\lambda = -50\,\text{MHz} \tag{3.4}$$

where μ_B denotes Bohr's magneton. This total detuning of **-350MHz** corresponds to ***-170MHz*** relative to the laser frequency.

3.5.2.5 Zeeman Slower Repumper

In regions of strong magnetic fields within the Zeeman slower, the distance between the cycling transition levels and the other energy levels is increased such that the loss process described in the penultimate section is strongly suppressed. Repumping is only necessary in the domain of the zero crossing of the magnetic field. In the rest frame of the atoms a change of the magnetic field changes the character of the light from σ^+ to σ^- and vice versa, thus, pumping from one outermost magnetic substate ($m_{F'} = 3$) to the other ($m_{F'} = -3$) is accomplished. During this repolarization process decays into the F=1 ground state are no longer forbidden. Consequently, it is here that the repumper has to act. The repumper needs to be detuned by +1713 MHz minus the Doppler shift at the point of the zero crossing. However, since it is directly modulated onto the Zeeman slowing beam as described in section 3.5.3 this Doppler shift drops out[16].

3.5.2.6 Imaging

When doing experiments with cold atoms most of the information on the system is derived from images. To take a picture ("absorption image") the atomic cloud is illuminated briefly with a weak collimated beam of resonant light (**+0MHz**, ***+180MHz***) and scatters photons proportional to its local particle density. This produces a shadow of the cloud that is recorded by a camera.

3.5.2.7 Transfer into a Magnetic Trap

As briefly discussed in section 3.4.2 the atoms need to be transferred to the low-field seeking $|2,2\rangle$ state before being transferred to the magnetic trap. Efficient transfer can be achieved by shining in σ^+-polarized light resonant to the F=2 to F'=2 transition after switching off the MOT. This transfers the atoms to the dark

[16] The Zeeman slower beam is - according to its working principle - on resonance all along the magnetic field, thus, especially at the zero field. Consequently, a repumping beam shifted by +1720MHz is resonant at that point, too.

$|\mathrm{F'}, \mathrm{m_{F'}}\rangle = |2, 2\rangle$ state, without any further heating. Therefore, light at **-58MHz** (***+122MHz***) is needed.

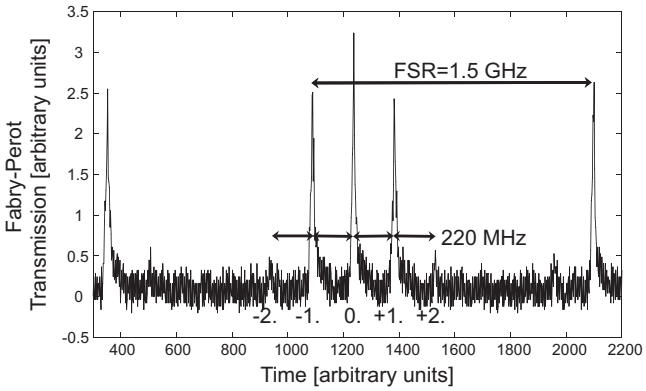

Figure 3.5: Transmission through a scanning Fabry-Perot interferometer with free spectral range (FSR) of 1500 MHz of a beam behind an EOM driven at 1720 MHz. Since the FSR is inferior to the mode spacing, the signal of the n-th sideband is folded back by a multiple of the FSR and appears at n times 220 MHz from the peak. The incoupled RF power was about 2.5 W.

3.5.3 Frequency Generation

All but two frequencies are shifted using acousto-optical modulators (AOM) fabricated by Crystal Technology Inc. These contain a radio frequency (RF) transducer attached to a transparent crystal of tellurium dioxide. Driving the transducer with RF powers of typically 0.5 W creates a running sound wave inside the crystal. Photons crossing the TeO_2 crystal will experience Raman processes, i.e. absorb or emit a phonon if the angle of incidence is such that quasi-momenta and energy is conserved. The photon's frequency can change in that way by integer multiples of the RF, where only the first orders are used in our experiment. Passing the light twice through one single AOM by retroreflecting results in a shift of twice the RF. Commercial standard AOMs are available typically at frequencies of 80, 110 and 200 MHz with bandwidths of about 10%. Our optics schemes have consequently been designed such that all high power beams are shifted by AOMs close to resonance, in order to achieve highest possible efficiencies. The AOMs used in a double-pass configuration have been set up similar to the proposition in [82].

Two exceptions concern the repumping light. For the MOT repumper we use an AOM at about 1.9 GHz provided by Brimrose Corporation of America (see figure 3.6). This device is far off from being standard and – to our knowledge –

can only be fabricated by the aforementioned company. Nominal efficiency is as high as 15%, however, the outcoupling aperture is too small. Since we need to recycle the zeroth order only 5% can be achieved without clipping at the housing. This is still sufficient for our purposes. For the Zeeman slower repumping light an electro-optical modulator (New Focus Inc.) with a center frequency of 1720 MHz is used. An incoupled RF-field is reinforced resonantly inducing a field dependent optical path by means of the Pockels effect. This sine shaped modulation creates sidebands to a laser beam passing through at $\pm nf$, where n is an integer and f is the radio frequency[17]. In figure 3.5 there is an example for what the spectrum looks like behind the EOM.

The drivers for these high frequency modulators have been assembled during this thesis and are briefly described in chapter E.

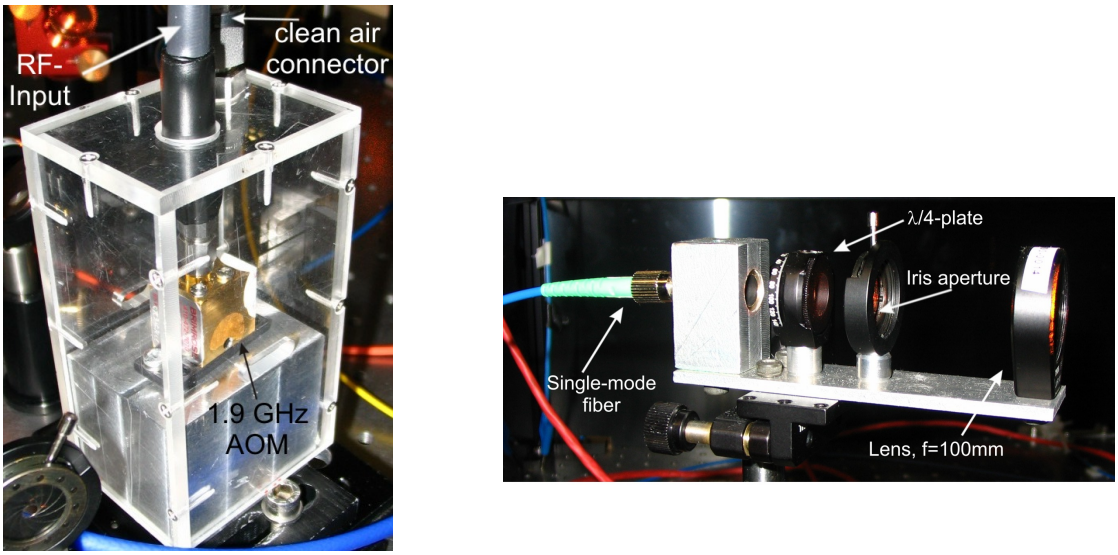

(a) (b)

Figure 3.6: *a)*: Acousto-optic modulator at 1.9 GHz. The housing has been manufactured in order to keep dust apart. *b)*: MOT beam assembly.

[17] The Power within the n-th sideband is proportional to $|J_n(\phi)|^2$, where ϕ is proportional to the square-root of the RF-Power and $J_n(\phi)$ denotes the n-th Bessel function.

3.5.4 The MOT setup

As mentioned in section 2.2, a MOT requires three pairs of beams with opposite circular polarizations[18] and a quadrupole field. The multi functional coils described in section 3.4 are also used for the magneto-optical trap. On the optical table the MOT light is coupled into a single-mode polarization maintaining fiber that is split into three pairs of fibers by a micro-optics device manufactured by Canadian Instruments[19]. While the power in two fibers of one pair is very close to equal ($\pm 2\%$), different pairs vary by up to 10%.

This fiber splitting unit greatly reduces the optics for the MOT - we only need to collimate the light and choose the right polarization. Therefore, a mount holding fiber holder, $\lambda/4$-plate and a 100 mm lens has been built (see figure 3.6).

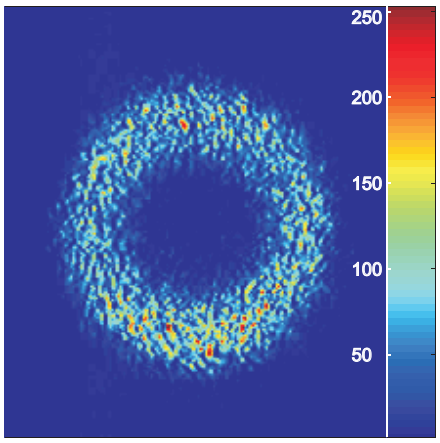

Figure 3.7: Dark spot

3.5.4.1 Repumping Light for Sodium and the Dark Spot MOT

The repumping light is coupled into a multimode fiber, mainly because the high frequency AOM destroys the Gaussian mode needed for efficient fiber coupling and no purified Gaussian mode is needed for repumping. In a further step, we will implement a so called dark spot MOT. As described in section 2.2.6 the number of

[18] Actually there are geometries requiring only four beams [83], however, achieving big stable MOTs like this is difficult.

[19] Actually a more power saving strategy is to retroreflect the MOT beams and to change the polarization using a $\lambda/4$-plate in front of the mirror. However, in an optically dense MOT the returning beam is attenuated and balancing might be a problem. In spite of this the group of van der Straten realized the biggest sodium MOT ever in this configuration [48].

atoms can be increased by a factor of ten by blocking the repumping light in the center of the MOT. By chance we found out that we can create a close to perfect ring-shaped mode by sloppily coupling into the multi-mode fiber. Focusing the laser beam into the incoupler (instead of collimating the beam) obviously excites whispering gallery type mode within the fiber cladding. The width of the ring structure can easily be tuned by displacing the focus relative to the incoupler. The incoupling exceeded 50% without any further optimization. If ever the core of the mode is not dark enough an additional aperture can be inserted without losing much power. The outcoupled structure is shown in figure 3.7. The ring is covered with a speckle pattern, even though we do not think that this will interfere one could remove it by "shaking" the fiber. The slightest movement of the fiber rotates the pattern, thus, a small loud speaker should suffice[20].

[20]Spatial filtering is an alternative, but breaks a butterfly on a wheel!

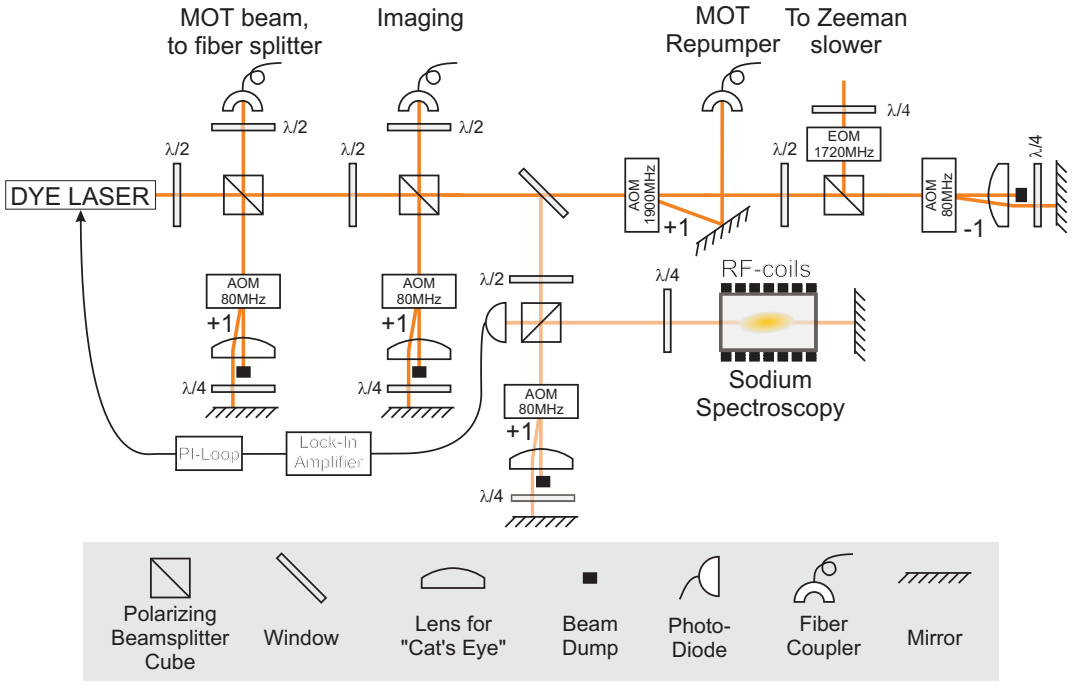

Figure 3.8: Overview of our sodium laser setup, the transfer beam for the magnetic trap has not yet been implemented.

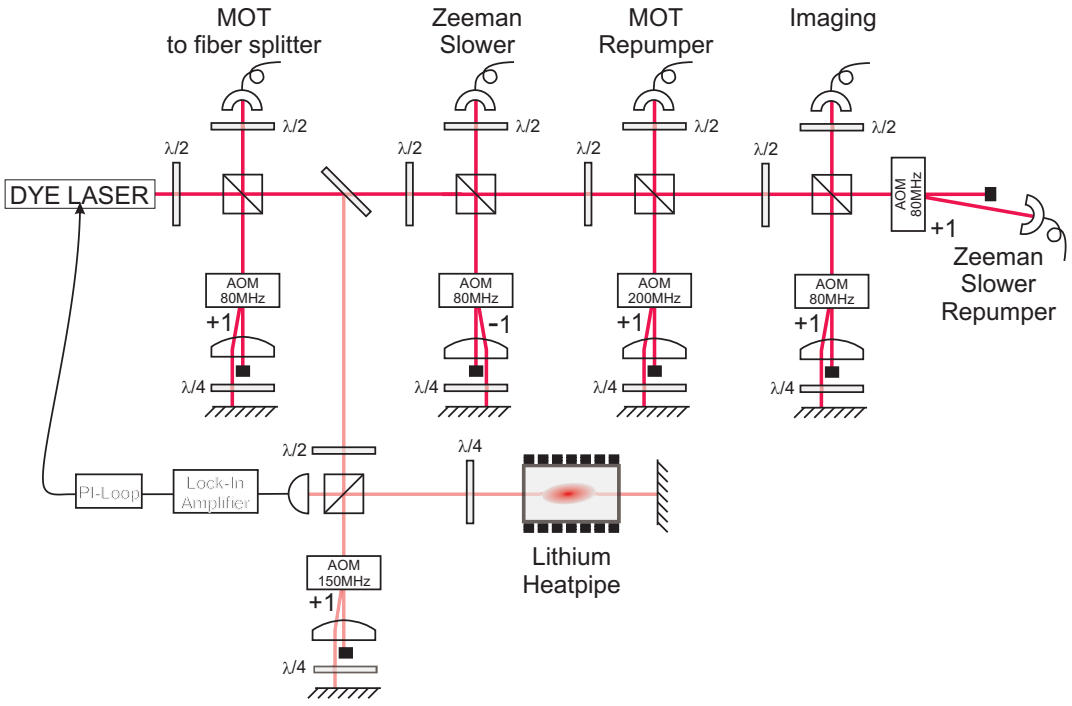

Figure 3.9: Draft of our lithium laser setup.

4 First Measurements

This chapter will give the first absorption measurements we have performed on our magneto-optical trap for sodium. More extensive studies are part of Marc Repp's diploma thesis [72]. Here we present the first absorption measurements on our MOT. All results we obtained have to be considered preliminary since this work has still been done using some provisional coils. In addition, systematic optimization of the different laser detunings, intensities and magnetic fields have not yet been done. One change compared to Marc Repp's diploma thesis is that the 1-on-6 fiber-splitter has been installed in the meantime. However the number of trapped atoms was still up to a factor of ten lower than before.

4.1 A Provisional Absorption Imaging System

4.1.1 Optical Density of an Atomic Cloud and the Beer-Lambert Law

Light crossing a sample of particles of density n is attenuated due to scattering processes according to the Beer-Lambert law, if the scattering cross section σ is independent of the light intensity:

$$I_t = I_0 \exp^{-\sigma n d} \tag{4.1}$$

where I_0 and I_t denote the incident and transmitted intensity respectively and d is the thickness of the sample.

The scattering cross section for atoms in a light field is given by [48]:

$$\sigma = \frac{\sigma_0}{1 + S + \left(\frac{2\delta}{\Gamma}\right)^2} \tag{4.2}$$

$$\text{where:} \quad \sigma_0 = \frac{\hbar\omega\Gamma}{2I_{sat}} \tag{4.3}$$

Here δ is the detuning of the light, Γ is the linewidth ($\Gamma = 2\pi \cdot 9.98\,\mathrm{MHz}$ for D_2-line of sodium), and $S = I/I_{sat}$ is the saturation parameter with the light intensity I and the saturation intensity I_{sat} for the given transition. σ_0 is called on-resonance cross section.

For atoms, the Beer-Lambert equation holds if:

$$\frac{1}{1 + S + \left(\frac{2\delta}{\Gamma}\right)^2} \overset{!}{\approx} 1 \tag{4.4}$$

Thus if the light intensity is small compared to the saturation intensity. Beyond, the scattering cross section decreases as a function of I. For resonant light of low intensity only σ_0 has to be known.

The optical density being defined as

$$\mathrm{OD} = \ln I_0/I_t \tag{4.5}$$

can now be related to the particle density using equations (4.5) and (4.1):

$$n = \frac{\mathrm{OD}}{\sigma d} \tag{4.6}$$

Given an absorption image (thus the optical density as a function of two spatial directions x and y, z being the direction of the imaging beam) the total particle number N can be calculated using:

$$N = \int_{-\infty}^{+\infty} \int_{-\infty}^{+\infty} \frac{\mathrm{OD}}{\sigma}\, dx\, dy \tag{4.7}$$

where the z direction ("d") just drops out since this integration has already been done implicitely when projecting the cloud onto the camera.

On a discrete grid, defined by the CCD pixels, the integral turns into a sum:

$$N = \sum_{n_x, n_y} \frac{\mathrm{OD}}{\sigma} \cdot A \tag{4.8}$$

where n_x, n_y denote the pixels of the whole image and A is the area of one pixel[1].

[1] This equation remains valid if there is some optical magnification, since the scattered light stays the same.

4.1.2 A Provisional Imaging System

A provisional absorption imaging system has been set up using a "PCO pixelfly vga" digital CCD camera system with a resolution of 12 bit. The dimension of one pixel is $9.9 \times 9.9\,\mu\mathrm{m}^2$. An imaging beam resonant to the atomic transition with very low intensity ($\approx 10\,\mu\mathrm{W/cm}^2$) compared to the saturation intensity has been installed. It passes through a single mode polarization maintaining fiber and is collimated on the vacuum table. Its angle of incidence onto the glass cell is about 20°. This reduces interference fringes due to multiple reflections within the glass cell.

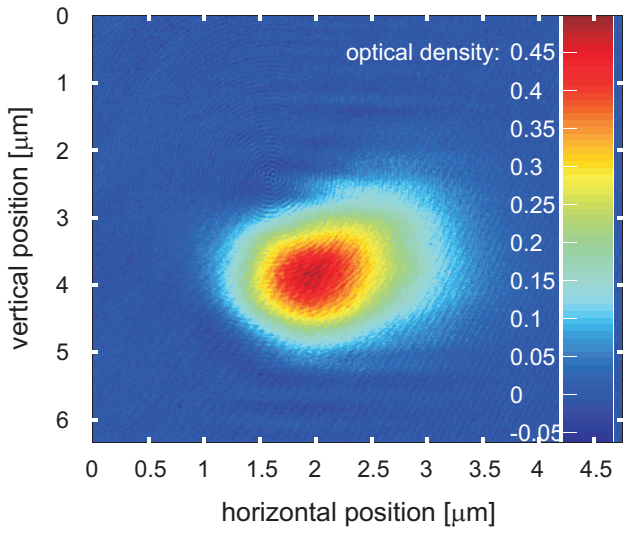

Figure 4.1: Optical density of the magneto-optical trap.

For a quantitative analysis of the atom number, three images – with atomic cloud, without atomic cloud and without imaging beam – have to be taken. The latter ("dark image") is subtracted from the others in order to compensate for any stray light and camera noise. The logarithm of the (point-by-point) ratio of the resulting two images gives the optical density per pixel.

4.2 Estimating the Atom Number in the Sodium MOT

The diameter of the MOT we have analyzed was on the order of 2 mm. The magnetic field gradient of the quadrupole field was below 10 G/cm, thus Zeeman shifts of the atoms are on the order of 2 MHz and thus negligible. Doppler effect (well below 1 MHz) does not play a role, either. Images have been taken with the magnetic quadrupole field still on[2]. For an estimate of the atom number any absorption properties depending on the quantization axis have not been taken into account in the following and the minimal saturation intensity has been used for calculations (for sodium: $I_{sat} = 6.2\,\mathrm{mW/cm^2}$ for the transition $|F, m_F\rangle \rightarrow |F', m'_F\rangle = |2, \pm 2\rangle \rightarrow |3, \pm 3\rangle$). Hence, the absorption image can directly be identified as the density distribution projected onto the CCD. At the same time, the number of particles is underestimated systematically.

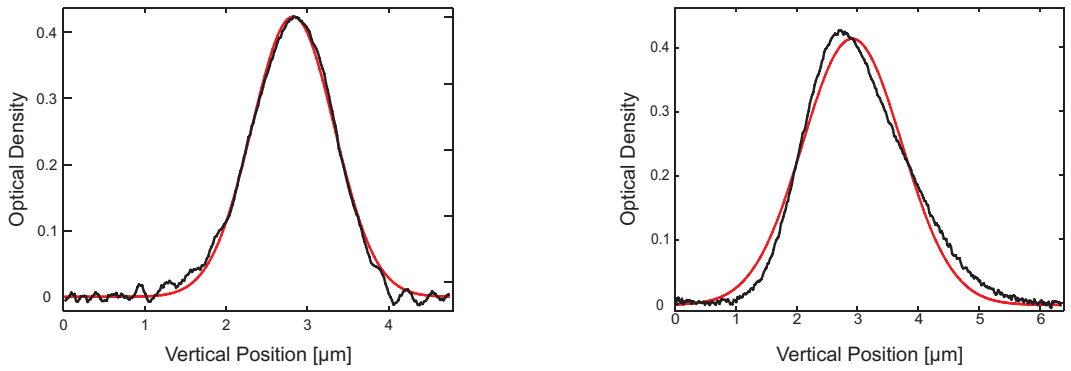

(a) (b)

Figure 4.2: Averaged column density profile (*a)* and row density profile (*b)*) shown in figure 4.1 together with Gaussian fits.

Figure 4.1 shows one of the first images taken, in figure 4.2 the averaged row and column density profiles are shown. Evidently, the optical density is low. Using equation (4.8) yields an atom number on the order of $2 \cdot 10^7$. A Gaussian plot to the line profiles yields diameters (FWHM) of $d_a = 1.20(2)\,\mathrm{mm}$ in vertical (axial) and $d_r = 1.92(2)\,\mathrm{mm}$ in horizontal (radial) direction. Evidently, the cloud has not a Gaussian shape in horizontal direction but the row profile is slightly tilted.

[2] Our interim coils could not be switched fast enough.

This may arise as soon as the effective potential of light and magnetic forces is no longer harmonic but contains higher order terms. Probably the Zeeman slower beam contained some close to resonant stray light pushing the magneto-optical trap slightly.

Assuming the cloud to have the same thickness in both radial directions the peak density in the center is given by:

$$n_{max} = \frac{8(\sqrt{\ln 2})^3 N}{\pi^{3/2} d_r^2 d_a^2} \approx 10^9 \,\mathrm{atoms/cm^3} \tag{4.9}$$

The low optical density indicates that multiple scattering processes do not yet play a dominant role. In this case atoms move in a quasi-harmonic potential [72, 84] and one would expect a Gaussian density distribution. This justifies the Gaussian fit in figure 4.2.

Refer to Marc Repp's [72] diploma thesis for loading and loss rates as well as temperature estimates.

5 Résumé and Outlook

5.1 Current Progress of the Experiment

One year ago, we started to set up an experiment on degenerate Fermi gases of ^{6}Li with bosonic ^{23}Na as a refrigerant. During this year, we have installed a laser system for cooling and trapping of ^{23}Na and a vacuum apparatus. Also a new lab has been equipped from zero (see page (iii)) . A first magneto-optical trap for sodium atoms with on the order of 10^8 atoms has been seen, however these results have to be considered as preliminary.

In the meantime the final coils together with working offset coils (for compensation of any stray magnetic fields) have been installed and the vacuum apparatus (formerly slightly bent), has been straightened. Furthermore, a running version of the computer control has just been released. Altogether, this should allow for increasing the number of trapped atoms drastically. Especially since from now on systematic optimization will be greatly simplified.

5.2 Outlook

An important milestone on our way to degeneracy will be the first BEC of sodium.

Before there are still some steps to take. First of all our multi function coils, installed since end of October 2007, need to be put into operation. Afterwards the first thing to do will be to increase the atom number within the magneto-optical trap using a dark spot technique and the transfer into the magnetic trap. Another ongoing project is the design and construction of the microwave antenna for 1.8 GHz and drivers that will be used for RF evaporative cooling.

Once the BEC has been obtained the lithium part will be tackled. For this purpose, the lithium laser system still needs to be set up. Yet the optics needed

is already available and this part should not take too much time. In parallel, a proper imaging system needs to be set up. Probably similar to the one installed in our rubidium BEC experiment next door [85]. A final thing is the transfer of the species to an optical dipole trap and this is where the actual experiment will begin...

A Sodium Data

A simplified level scheme of sodium can be found in figure 3.3. The vapor pressure is plotted in figure D.2.
Table A.1 finally lists some important optical properties of sodium. For further information refer to [64].

Frequency without Hyperfine-Shift	ω_0	$2\pi \cdot 508.848.716.2(13)\,\mathrm{THz}$
Transition Energy	$\hbar\omega_0$	$2.104\,428\,981(77)\,\mathrm{eV}$
Wavelength (Vacuum)	λ	$589.158\,3264(15)\,\mathrm{nm}$
Lifetime	τ	$16.249(19)\,\mathrm{ns}$
Natural Line Width (FWHM)	Γ	$2\pi \cdot 9.9795(11)\,\mathrm{MHz}$
Recoil Velocity	v_r	$2.9461\,\mathrm{cm/s}$
Recoil Temperature	ω_r	$2.3998\,\mu\mathrm{K}$
Doppler Temperature	T_D	$235\,\mu\mathrm{K}$
Saturation Intensity (cycl. transition)	I_{sat}	$6.2600(51)\,\mathrm{mW/cm^2}$

Table A.1: Sodium D_2 Transition Data [64].

B Atomic Beam Shutter

B.1 General Aspects

During this work, a driver for the atomic beam shutter has been realized. About 10 cm behind the oven nozzle there is a rotary feedthrough inserted into our vacuum system, that is connected to a thin plate made of stainless steel. Depending on the position, the atomic beam is blocked by it or not. The problem specifications were a sufficiently high shutter speed (shutting in much less than 1s) without striking the plate against the wall heavily.

The solution was to use a BLUEBIRD high-speed servo (model BMS-661 MG HS), typically used in model aircraft or cars. At a 6 V supply it is specified to be faster than 0.1 s for a 60° turn with no load. Maximal torque is 50 Ncm, more than sufficient for the small moment of inertia of the feedthrough plus the plate. Servos contain an electric motor, a gear and a position sensor. Choosing a position is done by sending a pulse width modulated (PWM) signal to the servo continuously, where 5% and 10% duty cycle correspond to the extreme positions. Frequency should typically be in the range of 50 to 100 Hz. An internal control circuit drives the servo to the selected position.

B.2 User Manual

B.2.1 Installation

Turn the servo arm such that the screws that are transmitting torque are accessible from behind, slightly screw (very few turns!) it to the rotary feedthrough and bring the shutter to a centered position. Afterwards clamp the shutter assembly to the vacuum apparatus. Make sure it is centered well.

B.2.2 Choosing Setpoints and Operation

Connect the driver box to the shutter assembly, to power supplies for the electronics (+5...+15 V) and servo (+4...+6 V, up to 1 A) and an alternating TTL signal of less than 1 Hz. The servo will start to switch between the two positions given by the potentiometers. Adjust them for complete blocking/passage of the atomic beam. Finally connect the TTL input to the computer control.

B.3 The Circuit

The electronics must provide the following features:

- two (analog) inputs corresponding to the user selectable setpoints "on" and "off"
- one TTL input switching between the two states
- one PWM output (to servo)
- one status output

The easiest way how to achieve this is by means of a small microcontroller. We chose a PIC 12F683 manufactured by Microchip with 8 pins and with 8-bitted data memory. It is equipped with 6 multifunction I/O pins, configurable as analog inputs or digital I/O. Especially it contains an internal clock oscillator and a PWM module[1][2].

In figure B.1 one can find the circuit now exhibiting a minimum of additional parts, namely two potentiometers (voltage dividers, R2 and R3), one voltage regulator for protection purposes of the microcontroller only (IC1) and a light emitting diode as status indicator. As a reference voltage of the internal 10 bit analog to digital converter the supply voltage is used (so setpoints actually do not depend on any fluctuations of the latter!).

B.4 Programming

The programming part has been done in Assembler. Implementation was done in a straightforward way, yielding as few debugging as possible. This section is

[1] For more details refer to the data sheet: `http://ww1.microchip.com/downloads/en/DeviceDoc/41211D_.pdf`

[2] A nice introduction to PIC microcontrollers can be found here: `http://www.sprut.de/electronic/pic/index.htm`

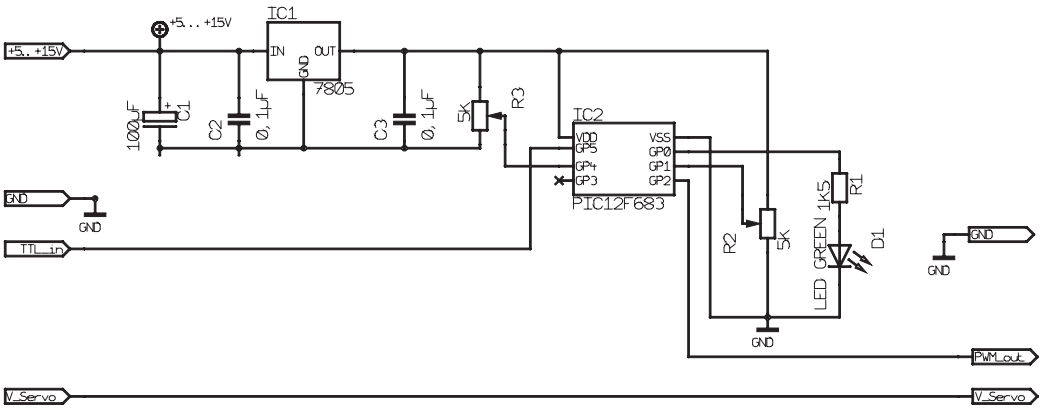

Figure B.1: Circuit of the atomic beam shutter driver

supposed to give a rough overview, for a more detailed documentation refer to the source code B.5.

In the "Init" part in- and outputs and their operational mode, as well as the A/D converters and the PWM module are configured; the clock-frequency is set to 1MHz. Refer to the source code header for further information on the pin assignment. The PWM module is connected to the internal Timer 2 module. Prescalers allow to reduce the PWM frequency to about 62 Hz. The Main function mainly contains an endless loop polling the TTL-input pin for changes. Whenever TTL-levels change, the LED is switched, the active A/D-port is toggled, triggered and one acquisition is accomplished. In a next step the result is divided by 16 (i.e. the result is shifted to the right four times) and incremented by 45. This value is written into the register governing the duty cycle. Together with a resolution of 10 bit of the PWM module this yields settable duty cycles between $45/1024 = 4.4\%$ and $(64+45)/1024 = 10.6\%$. Since the supply voltage is also used as the reference for the A/D-converter, the acquired value actually does not depend on any voltage changes. Finally the controller jumps back into the loop.

B.5 Source Code

```
{ list p=12f683
;*****************************************************************************
;
; Driver for atomic beam shutter
; of the NaLi-Experiment
; @ Kirchhoff-Institut für Physik, University of Heidelberg
; AG Oberthaler
;
;******************
;
; Connect a standard servo to Pin 5 (PWM-driven,
;     duty-cycle 5%-10%, 50Hz period)
; Connect voltage dividers to Pins 3 and 6
; Connect a Status-LED to Pin 7 (I_max=25mA)
; Connect 0V to Pin 1
; Connect +5V to Pin 8
;
; Choose the two setpoints by means of the voltage dividers
; The servo position may now be selected with TTL-Signals on Pin 2
;*****************************************************************************
;*      pin assignment
;*      --------------------------------
;*      Pin 7: GP0 > out 0,  LED-Status out
;*      Pin 6: GP1 > in 1,   A/D-in
;*      Pin 5: GP2 > out 2,  PWM-out
;*      Pin 4: GP3 > in 3,   MCLE-in
;*      Pin 3: GP4 > in 4,   A/D-in
;*      Pin 2: GP5 > in 5,   TTL-in
;*      Pin 1: 0V
;*      Pin 8: 5V (=V_ref for A/D-Conversion)
;*****************************************************************************
; Version: September 30th, 2007
; author:  Stefan Weis, stefan-weis@gmx.de
;
; processor:  PIC 12F683
; clock frequency:  1 MHz (internal)
;
;*****************************************************************************
; Include register names for the PIC 12F683

        #include <P12f683.INC>

; Configuration:
; power up timer, no watchdog, internal oscillator, masterclear enabled
        __CONFIG        _MCLRE_ON & _PWRTE_ON & _WDT_OFF & _INTOSCIO

;*****************************************************************************
; define variables
  Flags equ 0x20 ;LSB is set to present status of TTL-Input
temp  equ 0x21 ;for calculations

;*****************************************************************************
        org     0x00
        goto    Main

;*****************************************************************************
        org     0x04
                    ;Interrupt Routine, it might have been more elegant
                    ;using interrupts on change of Pin GP5, but this
                    ;direct implementation can be debugged more easily

;*****************************************************************************
; Initialization
```

```
;*********************************************************************
Init
  CLRF    Flags
  BANKSEL OSCCON
  bsf     OSCCON, IRCF2   ;set internal frequency to 1MHz
  bcf     OSCCON, IRCF1   ;
  bcf     OSCCON, IRCF0   ;
  bsf     OSCCON, SCS     ;activate internal clock


;SET PIN USAGE (I, O, analog, digital):

  BANKSEL GPIO            ;
  CLRF    GPIO            ;Init GPIO to zero
  BANKSEL TRISIO
  MOVLW   0x3A            ;Set GP<0,2> as outputs
  MOVWF   TRISIO          ;and set GP<1,3:5> as inputs

  BANKSEL ANSEL           ;
  CLRF    ANSEL           ;digital I/O
  MOVLW   0x7A            ;Set GP<1,4>, i.e. AN<1,3> as analogue inputs
  MOVWF   ANSEL           ;use internal clock for conversion

  BANKSEL ADCON0
  MOVLW   0x05            ;left justified (8 MSBs in ADRESH)
  MOVWF   ADCON0          ;A/D-Conversion on


;CONFIGURE PWM module:

  BANKSEL T2CON
  bsf     T2CON, T2CKPS1  ;prescaler
  bsf     T2CON, MR2ON    ;Timer2 started

  BANKSEL PR2
  MOVLW   0xFF
  MOVWF   PR2             ;PR2+Timer2 prescaler --> ~50Hz @ 1MHz Clock

  BANKSEL CCP1CON
  bsf     CCP1CON, CCP1M3 ;PWM chosen in
  bsf     CCP1CON, CCP1M2 ;mode active high
  bcf     CCP1CON, CCP1M1 ;

  return

;end of initialization

;*********************************************************************
;Main
;*********************************************************************
Main
  call    Init
  goto    chgd_to_high    ;in order to enable PWM on startup

loop
  BANKSEL GPIO
  btfsc   GPIO, 5         ;get TTL-Signal
  goto    chgd_to_high?   ;if high go to chgd_to_high?
  goto    chgd_to_low?    ;else go to chgd_to_low?

chgd_to_high?
  BANKSEL STATUS
  btfsc   Flags, 0        ;if Flag bit is also equal to one
  goto    loop            ;return to loop (no change!)

  BANKSEL ADCON0
```

```
  bsf     ADCON0, CHS1    ;choose A/D-Channel, wait for about 5
                          ;microseconds (i.e. 5cycles) until
                          ;multiplexing has been finished
  bsf     Flags, 0        ;set Flag bit to current TTL-level (=1)
  bsf     GPIO, 0         ;set Status indicator (LED) to high (="on")
  goto    Changed         ;else run Changed function

chgd_to_low?
  BANKSEL STATUS
  btfss   Flags, 0        ;if Flag bit is also equal to zero
  goto    loop            ;return to loop (no change!)

  bcf     ADCON0, CHS1    ;choose A/D-Channel, wait for about 5
                          ;microseconds (i.e. 5cycles) until
                          ;multiplexing has been finished
  bcf     Flags, 0        ;set Flag bit to current TTL-level (=0)
  bcf     GPIO, 0         ;set Status indicator (LED) to high (="off")
  goto    Changed         ;else run Changed function

Changed
  NOP
  BANKSEL STATUS          ;5 cycles finished

  BSF     ADCON0, GO      ;Start conversion
  BTFSC   ADCON0, GO      ;Is conversion done?
  GOTO    $-1             ;No, test again

  BANKSEL ADRESH          ;8 MSBs of conversion contained in ADRESH

;  rescaling to duty cycle range of Servo will be done in the following
;  for 5% to 10% duty cycle rounding to 6 significant bits will be
;  effectuated in the following, i.e. discard the two least
;  significant bits, rotation to the right twice yields 64/1024=6.25%
;  range adding 45=0x2D yields a range of 45/1024=4.4% to 99/1024=9.7%

  RRF     ADRESH, 1       ;rotating right
  RRF     ADRESH, 1       ;rotating right
  bcf     ADRESH, 6       ;clear two...
  bcf     ADRESH, 7       ;...most significant bits
  movlw   0x2D            ;add...
  ADDWF   ADRESH, 1       ;... 45

  SWAPF   ADRESH, 0       ;two least significant bits of result have to be
                          ;written into CCP1CON<4:5>
  movwf   temp            ;swapped and modified bits in temp are...
  bsf     temp, 3         ;...
  bsf     temp, 2         ;...
  bcf     temp, 1         ;...
  MOVFW   temp            ;written into CCP1CON...
  MOVWF   CCP1CON         ;without changing configuration bits.

  rrf     ADRESH, 1       ;Eliminate two LSBs of result...
  rrf     ADRESH, 1       ;...that have already been treated
  bcf     ADRESH, 7       ;clear two...
  bcf     ADRESH, 6       ;...most significant bits
  movfw   ADRESH          ;and put result...
  movwf   CCPR1L          ;into CCPR1L
  goto    loop
}
```

C Beam Profiler

During this diploma thesis software for a custom made beam profiler[1] has been developed. Electronics and the CCD-chip have been taken from a Logitech QuickCam Pro 4000 webcam and put into a housing made of brass. Thereby lenses and infrared filters have been removed. The software for MATLAB captures images from the camera continuously, fits and plots them and provides further functionality described in the following section.

C.1 Application Notes

C.1.1 Warnings

- *This program uses the MATLAB "Image Acquisition Toolbox", make sure this add-on is installed; furthermore the application is relatively performance consuming. In order to obtain a reasonable frame rate use an up-to-date PC.*

- *This is not a high precision solution, even though some comparisons to more precise methods have demonstrated accuracies of better than 5%, if the following precautions are met.*

- *Whenever the chip is close to saturated, waists are overestimated. So try to keep gray values below 150.*

- *The CCD and the absorber in front do not sustain infinitely much intensity, make sure to reduce the power contained in the beam to a reasonable value.*

- *Whenever you execute the live_BeamProfiler.m file the camera driver enables the property "Mich verfolgen" within the control panel. This feature tries to center somebody's face onto the captured images, so pretty useless in this*

[1] Built by Tobias Schuster.

case. However, it seems to be impossible to change this default setting, so do not forget to uncheck it.

C.2 Functionality

C.2.1 Overview, Graphs and Fitting

After connecting the beam profiler and – if required – installing the driver software, start the "live_BeamProfiler" m.-file. You'll see the graphical user interface (GUI) shown in figure C.1. First select the color channel that gives the best results / fits your laser color using the radiobuttons. Afterwards make sure the peak gray values are neither close to saturated nor too low, by either changing the light intensity or choosing an adequate setting of the exposure time and sensitivity in the camera's control panel. By default the GUI shows three graphs, that are updated about three times per second (depending on your computer's performance): On the upper left a false color image is shown, on the bottom left / right a signal proportional to the row / color sum of the image is shown as well as a Gaussian fit to the profile.

This summation has been done in order to smooth the curve that is fitted. For a perfect two-dimensional Gaussian beam, this yields the same results since integrations along the x- or y- axis are independent providing only a constant factor. If you are only interested in a visual examination of the beam the button "fitting?" disables the fitting procedure leading to an increased repetition rate. For very noisy images put the slider "averaged" to a higher value.

C.2.2 Reducing Stripes and Saving Results

In case you are using infrared lasers (e.g. Nd:YAG) there may vertical stripes appear, that perturb the fitting. Use the "reduce stripes" functionality to get rid of them, if your beam is not too big in the vertical direction. After fitting the y-direction, the algorithm averages over all rows that are not hit by the beam. This row profile is subtracted from the x lineprofile afterwards. Finally the button "Save current frame" allows to save the current image to a Windows bitmap file. The "Log fitting results to file" button starts logging the fitting parameters (i.e. waist in x- and y- direction, x- and y- coordinate of the center of the fitted Gaussian) selected in the subsequent dialog to a user specified text file, e.g. for an analysis of the pointing stability of the laser.

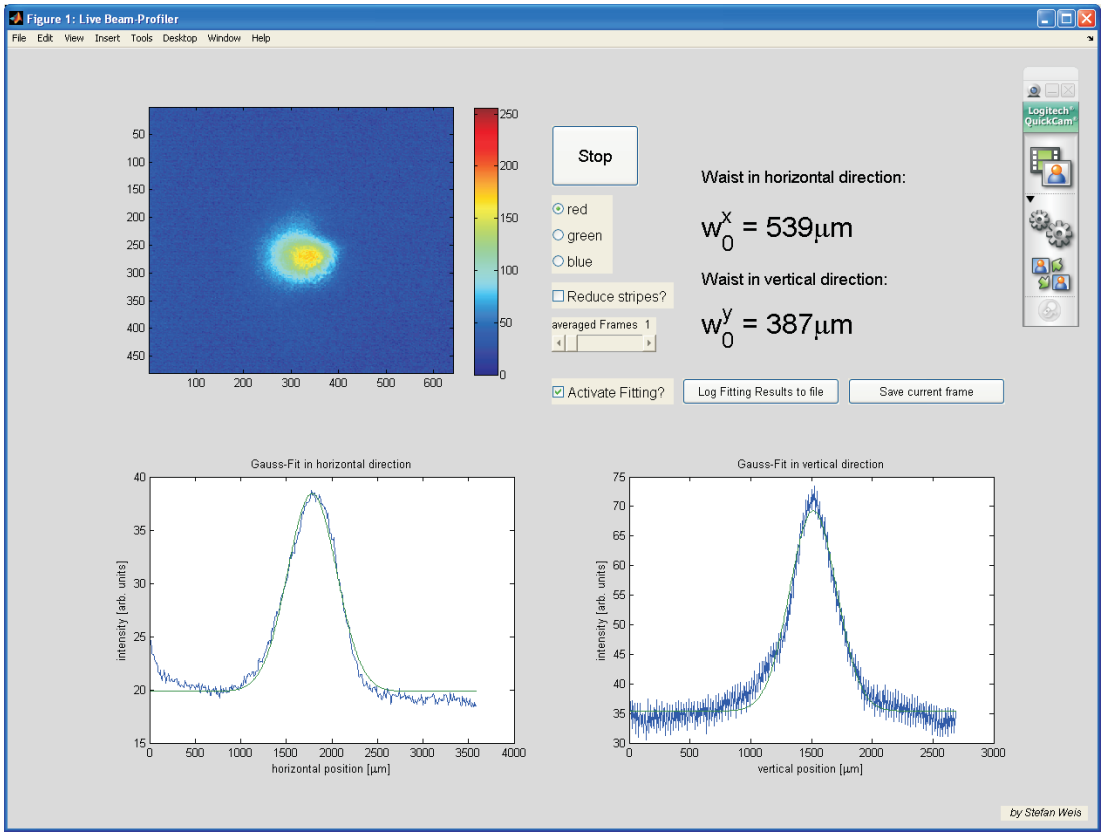

Figure C.1: Screenshot of the Beam Profiler

C.3 Some Comments on the Programming and Fitting

Since there is no Windows XP low-level driver available for this camera, the winvideo interface of the operating system had to be used. This provides only some basic configurations concerning trigger modes and resolution. The winvideo interface acquires its data from the camera driver. The aforementioned control panel influences parameters like exposure time, sensitivity or any gamma corrections. Unfortunately, gray values are no longer proportional to the intensity but the slope flattens for higher gray values.

Available video devices can be found using:

```
>> imaqhwinfo
```

Acquiring images from any (?) video source can be obtained using the MAT-

LAB videoinput functionality, e.g.:

```
>> vid=videoinput('winvideo', 1, 'RGB24_640x480')
```

Available trigger settings can be found using

```
>> set(vid)
```

For manual triggers one obtains the acquired image (sequence) using:

```
>> trigger(vid)
>> color_image=getdata(vid,1)
```

For more details, refer to the MATLAB Help topic "Basic Image Acquisition Procedure". The fitting procedure uses a slightly modified version (any warnings have been suppressed) of the "fminsearch" function, where starting values are estimated based on the maximal and minimal values found within the smoothed line profiles together with their position plus a roughly estimated half width. Within the source code, you can find a more detailed description.

D Spectroscopy Cell and Doppler-Free Laser Locking

Locking the sodium dye laser is done by means of a Doppler-free saturated absorption spectroscopy. Therefore, resonant light passes a sodium vapor cell twice. The pump beam saturates an atomic transition for atoms of a certain velocity v, whereas the counterpropagating probe beam excites atoms of velocity $-v$. Evidently, both beams do not interact as long as $v \neq 0$. For $v = 0$ a so-called lamb-dip appears, showing the Doppler-free profile of the line. See figure 3.8 for the optics scheme used for locking.

D.1 The Spectroscopy Cell

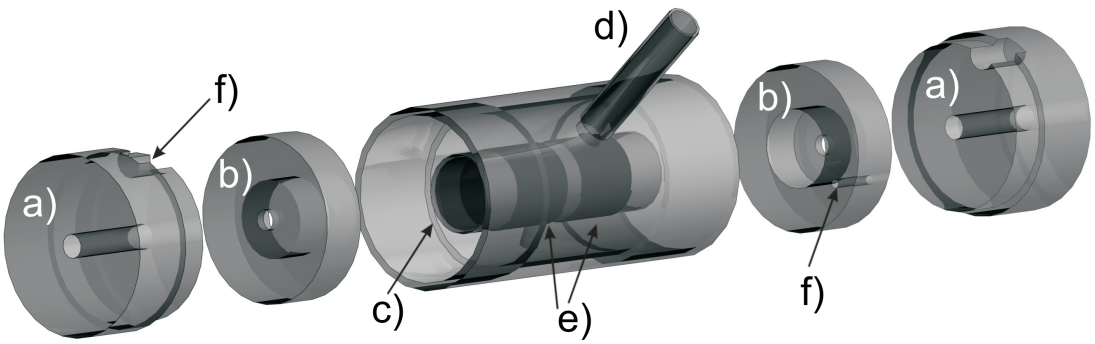

Figure D.1: Schematic drawing of the sodium spectroscopy cell, *a)*: end caps reducing the solid angle, *b)*: takes up the glass cell, *c)*: evacuated glass cell filled with sodium, *d)*: viewport, might also serve as a cold spot (not examined in detail), *e)*: RF-coils (feedlines not shown), *f)* aperture for included thermo couple (type K, not shown), *not shown*: heating coils.

The vapor pressure (cf. figure D.2) for sodium needs to be increased in order to

obtain a sufficient absorption signal. Therefore, a small oven has been developed and built during this thesis. A drawing can be found in figure D.1. It takes a glass cell filled with sodium (Thorlabs CP25075-NA). The solid angle of the aperture has been minimized in order to avoid heat-sinking effects at the windows leading to steaming up with sodium. Yet this cannot be completely suppressed and transparency diminishes after a while. In this case, windows can be cleared by covering them with some aluminum foil and heating up the oven to temperatures close to 200°C for half an hour. The sodium mirror will disperse increasing the transmission of the windows. The oven can be heated up with a solenoid put onto the aluminum cylinder (not shown in figure D.1). The windings are two at a time in opposite direction avoiding magnetic fields. Magnetic fields in the center of the oven are well below 0.5 G for 2 A of heating current. A temperature of about 130°C has shown to be optimal for spectroscopy, representing a tradeoff between the size of the signal and optical transmission, where 130°C correspond to about 1.9 A/18 V electrical power in steady state. In figure D.3 a theoretical calculation[1] shows the transmission of an incident beam for several saturation parameters S.

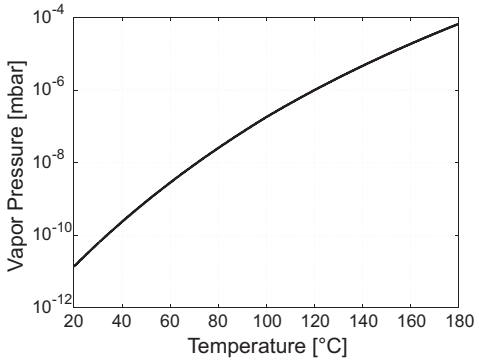

Figure D.2: Vapor Pressure of sodium as a function of temperature [64].

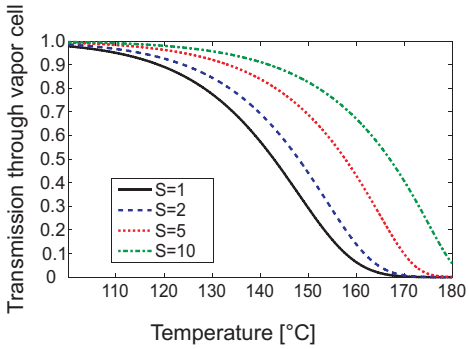

Figure D.3: Transmitted intensity as a function of temperature for different saturation values

D.2 Lock-in Scheme

Directly onto the glass cell RF-coils for a high-frequency modulation of the magnetic Zeeman sublevels have been wound. They are designed such that together

[1] Numerical integration of the absorption along the axis. The non-linearity of the absorptional cross section has been taken into account.

with a 30nF capacitor in a series LC circuit amplitudes of up to $B = 6$G at the resonance frequency of about 80 kHz can be obtained using a standard Voltcraft type 7202 wobbel function generator. See figure D.4 for an explanation. This modulation is detected on the photodiode and fed into a lock-in amplifier, giving rise to an output signal proportional to the derivative of the Doppler-free spectrum (cf. figure D.4 for a schematic). The measured sodium spectrum is shown in figures D.5 and D.6.

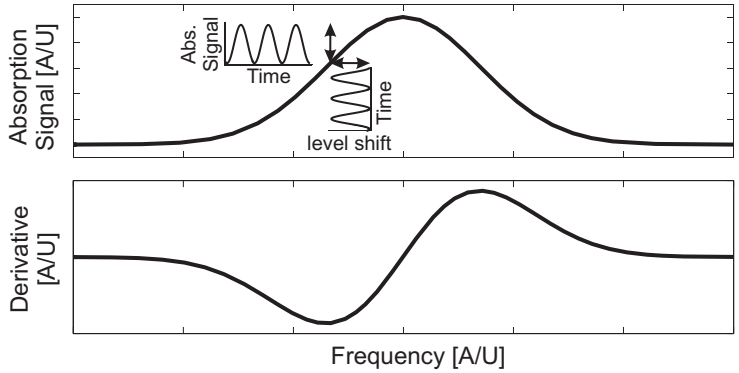

Figure D.4: *Working principle of the lock-in scheme*: The upper graph shows a schematic of a resonance line. The latter is shifted up and downwards by means of a RF magnetic field. In the frame of the atoms, the laser frequency is modulated relative to their resonance frequency leading to a modulated absorption signal. Feeding this signal into a lock-in amplifier yields an output signal proportional to the modulation amplitude, i.e. the derivative of the line. Locking on top of the line can now be accomplished by feeding this signal - in this framework also referred to as error signal - back into a control circuit.

Windings	140
Radius of Solenoid	12.5 mm
Length of Solenoid	55 mm
Inductance measured / theoretical	0.17 mH / 0.18 mH
Resonance Frequency with 27 nF in series	74.2 kHz
Peak magnetic Field at resonance[2]	6 G

Table D.1: Characteristics of the RF coil

[2]using a Voltcraft 7202 wobbel function generator

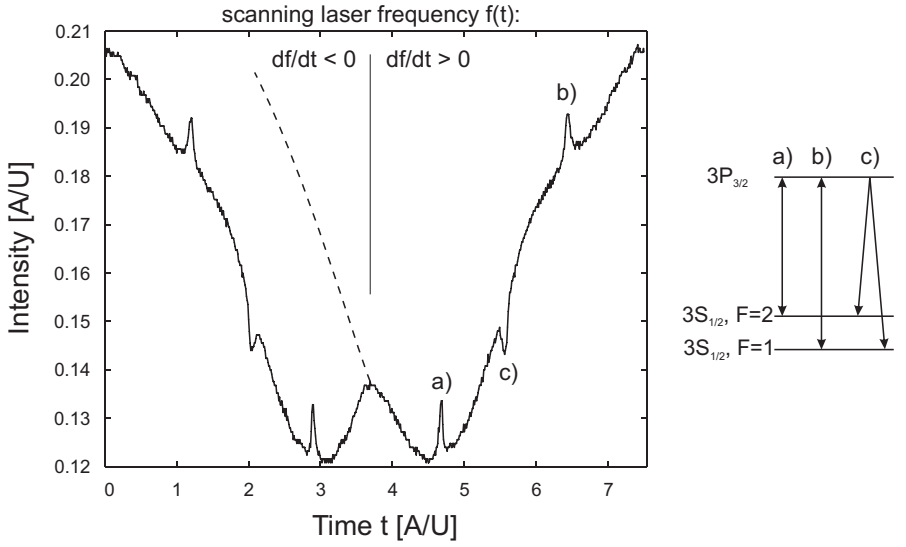

Figure D.5: D_2-line of sodium with the transitions *a)*: $3S_{1/2},\ F = 2 \rightarrow 3P_{3/2}$, *b)*: $3S_{1/2},\ F = 1 \rightarrow 3P_{3/2}$ and the cross-over line *c)*. The dashed line completes the Doppler profile of the line schematically.

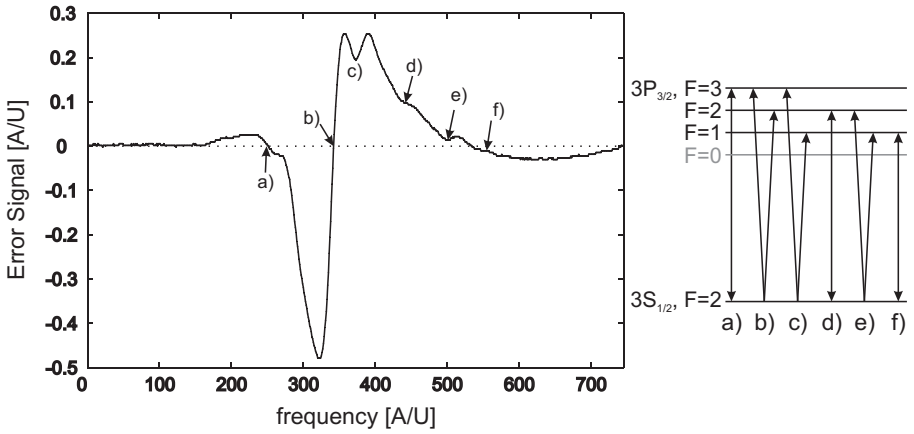

Figure D.6: Error signal (i.e. derivative) of the transition $3S_{1/2},\ F = 2 \rightarrow 3P_{3/2}$ with partially resolved hyper-fine structure of the excited state. Locking is done on the cross-over peak of the $F = 2 \rightarrow F' = 2/F' = 3$ transitions *(b))*. *a)*: $F = 2 \rightarrow F' = 3$, *c)*: cross-over $F = 2 \rightarrow F' = 1/F' = 3$, *d* $F = 2 \rightarrow F' = 2$, *e)*: cross-over $F = 2 \rightarrow F' = 1/F' = 2$, *e*: $F = 2 \rightarrow F' = 1$

E RF-Drivers for High-Frequency Components

For driving the high frequency AOM at 1859GHz and the EOM at 1713GHz a drivers have been set up. A schematic can be found in figure E.1 containing a list of levels, attenuations and gains for each component - VCO[1].

Since these two items are the most expensive objects on our optics table special care has been taken that the maximal specified RF powers of 4 W for the EOM and 1 W for the AOM cannot be exceeded under any circumstances. The output power has been measured using a Tektronix TDS 7254 oscilloscope with a 50Ω input impedance.

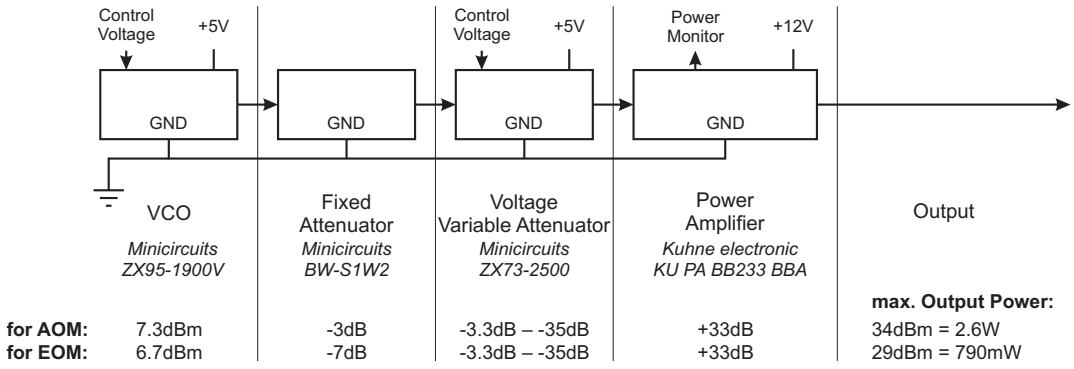

Figure E.1: Schematic of the RF drivers used for the high frequency AOM and EOM. Below a summary of the levels, attenuations and gains for each component is listed.

The power amplifiers feature a power monitor output. This voltage V_P is related to the RF-power P_{RF} as can be seen in figure E.2. A quadratic fit (valid

[1]Voltage Controlled Oscillator

for the frequency range between 1700MHz and 1900MHz) yields:

$$P = a_0 V_P^2 + a_1 V_P + a_2 \tag{E.1}$$

where $a_0 = 0.48\,\mathrm{W/V^2}$, $a_1 = 0.18\,\mathrm{W/V}$ and $a_2 = 0.02\,\mathrm{W}$. The driver electronics is connected to the crystals by means of a Minicircuits CBL-6FT-SMSM coaxial cable.

The VCO control voltage needs to be sufficiently stable compared to the natural linewidth of sodium. For a stability to about 1MHz the control voltage must not vary by more than ±15mV. Therefore a tunable voltage reference has been set up using a μA723 precision voltage regulator according to the application information "Basic High-Voltage Regulator" in the datasheet[2].

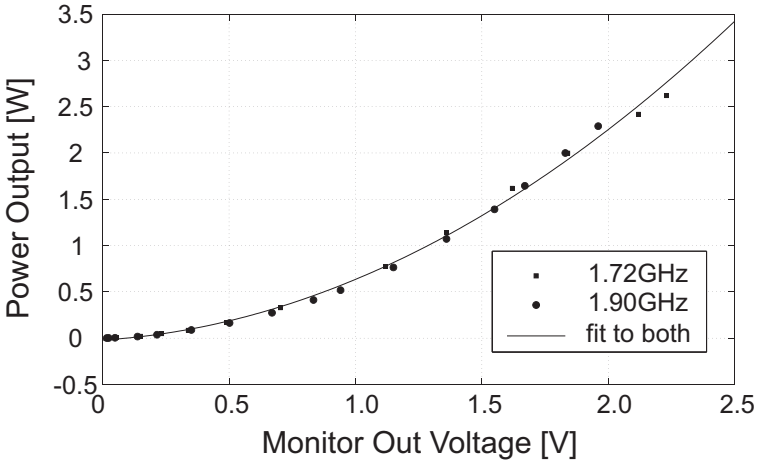

Figure E.2: RF power as a function of the monitor out voltage.

[2] `http://focus.ti.com/lit/ds/symlink/ua723.pdf`

F Danksagung

An dieser Stelle möchte ich mich bei allen Personen bedanken, die zum Gelingen dieser Arbeit beigetragen haben. Mein spezieller Dank gilt dabei:

- Prof. Markus K. Oberthaler für die Aufnahme in seine Arbeitsgruppe und die Möglichkeit, dieses neue, faszinierende Experiment mit aufzubauen. Nicht nur sein Enthusiasmus für Physik, die vielen wertvollen Diskussionen und die langen Nächte im Labor mit ihm, sondern auch zahlreiche Abende außerhalb des Labors machten dieses Jahr zu einem schönen und sehr wertvollen Jahr.

- Prof. Annemarie Pucci für die Begutachtung dieser Arbeit.

- Peter Krüger, dem wissenschaftlichen Leiter dieses Experiments, den Pionieren dieses Experiments Marc Repp, Jan Krieger und Jens Appmeier, sowie Elisabeth Brama und Anton Piccardo-Selg, die kürzlich zu uns gestoßen sind. Danke für die vielen schönen und lehrreichen Stunden im Labor und außerhalb!

- der gesamten Arbeitsgruppe für die Hilfe, die ich während des Jahres erfahren habe, die unterhaltsamen Kaffeepausen[1] und die gemeinsamen Abende beim Grillen, Beachvolleyball und Karten spielen.

- dem NaLi-Team, besonders aber Peter Krüger und Jan Krieger, für das Korrekturlesen meiner Arbeit.

- Mein Dank geht auch an die elektronische und mechanische Werkstatt des Instituts, insbesondere an Herrn Spiegel und Herrn Herdt, sowie die Glasbläserei des Physikalischen Instituts.

- meinen Eltern, die mich immer unterstützt haben und für mich da waren. Ohne Euch wäre dieses Studium so nicht möglich gewesen.

[1] `www.wikipedia.de`, `www.wikipedia.org`

- meiner Freundin Iris für die Geduld, Unterstützung und die wundervolle Zeit.

Bibliography

[1] S.N. Bose. Plancks Gesetz und Lichtquantenhypothese. *Z. Phys.*, 26:178, 1924.

[2] A. Einstein. Quantentheorie des Einatomigen Idealen Gases. *Kgl. Preuss. Akad. Wiss.*, 22:178, 1924.

[3] A. Einstein. Quantentheorie des Einatomigen Idealen Gases. Zweite Abhandlung. *Sitzungsber. Kgl. Preuss. Akad. Wiss.*, page 3, January 1925.

[4] M.H. Anderson, J.R. Ensher, M.R. Matthews, C.E. Wieman, and E.A. Cornell. Observation of Bose-Einstein Condensation in a Dilute Atomic Vapor. *Science*, 269(5221):198, July 1995.

[5] K.B. Davis, M.O. Mewes, M.R. Andrews, N.J. van Druten, D.S. Durfee, D.M. Kurn, and W. Ketterle. Bose-Einstein Condensation in a Gas of Sodium Atoms. *Phys. Rev. Lett.*, 75(22):3969, Nov 1995.

[6] W Pauli. The Connection Between Spin and Statistics. *Phys. Rev.*, 58:716–722, 1940.

[7] L.V. de Broglie. *Recherches sur la Théorie des Quanta*. PhD thesis, Sorbonne, Paris, 1924.

[8] R. Gati, B. Hemmerling, J. Fölling, M. Albiez, and M.K. Oberthaler. Noise Thermometry with Two Weakly Coupled Bose-Einstein Condensates. *Physical Review Letters*, 96(13):130404, April 2006.

[9] M. Albiez, R. Gati, J. Fölling, S. Hunsmann, M. Cristiani, and M.K. Oberthaler. Direct Observation of Tunneling and Nonlinear Self-Trapping in a Single Bosonic Josephson Junction. *Physical Review Letters*, 95(1):010402, June 2005.

[10] K. Xu, Y. Liu, J.R. Abo-Shaeer, T. Mukaiyama, J.K. Chin, D.E. Miller, W. Ketterle, K.M. Jones, and E. Tiesinga. Sodium Bose-Einstein condensates in an Optical Lattice. *Physical Review A*, 72(4):043604, October 2005.

[11] D. Rychtarik, B. Engeser, H.C. Nägerl, and R. Grimm. Two-Dimensional Bose-Einstein Condensate in an Optical Surface Trap. *Physical Review Letters*, 92(17):173003, 2004.

[12] M.R. Matthews, B.P. Anderson, P.C. Haljan, D.S. Hall, C.E. Wieman, and E.A. Cornell. Vortices in a Bose-Einstein Condensate. *Phys. Rev. Lett.*, 83(13):2498, Sep 1999.

[13] B. Demarco and D.S. Jin. Exploring a quantum degenerate gas of fermionic atoms. *Physical Review*, 58:4267, December 1998.

[14] B. Demarco and D.S. Jin. Onset of Fermi Degeneracy in a Trapped Atomic Gas. *Science*, 285(5434):1703, September 1999.

[15] H. Feshbach. Unified Theory of Nuclear Reactions. *Reviews of Modern Physics*, 36:1076, October 1964.

[16] C. Stan. *Experiments with Interacting Bose and Fermi Gases.* PhD thesis, Massachusetts Institute of Technology, 2005.

[17] B. Marcelis, E.G.M. van Kempen, E.G.M. Verhaar, and S.J.J.M.F. Kokkelmans. Feshbach Resonances with Large Background Scattering Length: Interplay with Open-Channel Resonances. *Physical Review A*, 70(1):012701, 2004.

[18] I. Bloch, J. Dalibard, and W. Zwerger. Many-Body Physics with Ultracold Gases. *ArXiv e-prints*, 704, April 2007.

[19] J.P. Gaebler, J.T. Stewart, J.L. Bohn, and D.S. Jin. P-Wave Feshbach Molecules. *Phys. Rev. Lett.*, 98:200403, 2007.

[20] M.J. Holman and P.A. Wiegert. Long-Term Stability of Planets in Binary Systems. *Astronomical Journal*, 117:621, jan 1999.

[21] E.P. Gross. Hydrodynamics of a Superfluid Condensate. *Journal of Mathematical Physics*, 4:195, February 1963.

[22] E.P. Gross. Structure of a quantized vortex in boson systems. *Nuovo Cimento*, 20(3):454, 1961.

[23] L.P. Pitaevskii. Vortex Lines in an Imperfect Bose Gas. *Sov. Phys. JETP.*, 13, 1961.

[24] S. Diehl. *The BCS-BEC Crossover in Ultracold Fermion Gases.* PhD thesis, University of Heidelberg, 2006.

[25] S. Flörchinger. Renormierungsgruppe von Quantenfeldtheorie bis Quantenstatistik. Exposé for a PhD-Thesis, 2007.

[26] M.E. Peskin and D.V. Schroeder. *An Introduction to Quantum Field Theory.* ABP, 1995.

[27] W. von der Linden. A Quantum Monte Carlo Approach to Many-Body Physics. *Physics Reports*, 220:53, nov 1992.

[28] G.E. Astrakharchik, J. Boronat, J. Casulleras, and S. Giorgini. Equation of State of a Fermi Gas in the BEC-BCS Crossover: A Quantum Monte Carlo Study. *Physical Review Letters*, 93(20):200404, November 2004.

[29] G.B. Partridge, W. Li, Y.A. Liao, and R.G. Hulet. Pairing, Phase Separation, and Deformation in the BEC-BCS Crossover. *Journal of Low Temperature Physics*, 148:323, August 2007.

[30] Y.I. Shin, C.H. Schunck, A. Schirotzek, and W. Ketterle. Phase Diagram of a Two-Component Fermi Gas with Resonant Interactions, 2007.

[31] J.E. Thomas, J. Kinast, and A. Turlapov, editors. *Universal Thermodynamics of a Strongly Interacting Fermi Gas*, 2006.

[32] M. Mark, F. Ferlaino, S. Knoop, J.G. Danzl, T. Kraemer, C. Chin, H.C. Nägerl, and R. Grimm. Spectroscopy of Ultracold Trapped Cesium Feshbach Molecules. *Physical Review A*, 76(4):042514, 2007.

[33] M.J. Wright, S. Riedl, A. Altmeyer, C. Kohstall, E.R. Sanchez Guajardo, J. Hecker Denschlag, and R. Grimm. Finite-Temperature Collective Dynamics of a Fermi Gas in the BEC-BCS Crossover. *Physical Review Letters*, 99(15):150403, 2007.

[34] D.S. Petrov, G.E. Astrakharchik, D.J. Papoular, C. Salomon, and G.V. Shlyapnikov. Crystalline Phase of Strongly Interacting Fermi Mixtures. *Physical Review Letters*, 99(13):130407, 2007.

[35] T. Bourdel, L. Khaykovich, J. Cubizolles, J. Zhang, F. Chevy, M. Teichmann, L. Tarruell, S.J.J.M.F. Kokkelmans, and C. Salomon. Experimental Study of the BEC-BCS Crossover Region in Lithium 6. *Physical Review Letters*, 93(5):050401, 2004.

[36] C.A. Stan, M.W. Zwierlein, C.H. Schunck, S.M. Raupach, and W. Ketterle. Observation of Feshbach Resonances between Two Different Atomic Species. *Physical Review Letters*, 93(14):143001, sep 2004.

[37] C. Ospelkaus, S. Ospelkaus, L. Humbert, E. Ernst, K. Sengstock, and K. Bongs. Ultracold heteronuclear molecules in a 3d optical lattice. *Physical Review Letters*, 97(12):120402, 2006.

[38] K.B. Davis, M.O. Mewes, and W. Ketterle. An Analytical Model for Evaporative Cooling of Atoms. *Appl. Phys. B*, 60:155, 1995.

[39] M. D. Barrett, J. A. Sauer, and M. S. Chapman. All-Optical Formation of an Atomic Bose-Einstein Condensate. *Phys. Rev. Lett.*, 87(1):010404, Jun 2001.

[40] C.J. Myatt, E.A. Burt, R.W. Ghrist, E.A. Cornell, and C.E. Wieman. Production of Two Overlapping Bose-Einstein Condensates by Sympathetic Cooling. *Phys. Rev. Lett.*, 78(4):586, Jan 1997.

[41] W. Zhang, C.A. Sackett, and R.G. Hulet. Optical Detection of a Bardeen-Cooper-Schrieffer Phase Transition in a Trapped Gas of Fermionic Atoms. *Physical Review A*, 60:504, July 1999.

[42] Z. Hadzibabic, C.A. Stan, K. Dieckmann, S. Gupta, M.W. Zwierlein, A. Görlitz, and W. Ketterle. Two-Species Mixture of Quantum Degenerate Bose and Fermi Gases. *Phys. Rev. Lett.*, 88(16):160401, Apr 2002.

[43] G. Roati, F. Riboli, G. Modugno, and M. Inguscio. Fermi-bose quantum degenerate $^{40}k - ^{87}rb$ mixture with attractive interaction. *Phys. Rev. Lett.*, 89(15):150403, Sep 2002.

[44] T. Fukuhara, Y. Takasu, M. Kumakura, and Y. Takahashi. Degenerate Fermi Gases of Ytterbium. *Physical Review Letters*, 98(3):030401, 2007.

[45] J.J. Zirbel, K.K. Ni, S. Ospelkaus, J.P. D'Incao, C.E. Wieman, J. Ye, and D.S. Jin. Collisional Stability of Fermionic Feshbach Molecules, 2007.

[46] M. Bartenstein, A. Altmeyer, S. Riedl, R. Geursen, S. Jochim, C. Chin, J. Hecker, R Grimm, A. Simoni, E. Tiesinga, C.J. Williams, and P.S. Julienne. Precise Determination of $6̂$Li Cold Collision Parameters by Radio-Frequency Spectroscopy on Weakly Bound Molecules. *Physical Review Letters*, 94:103201, 2005.

[47] C.A. Regal, M. Greiner, and D.S. Jin. Lifetime of Molecule-Atom Mixtures Near a Feshbach Resonance in 40K, 2003.

[48] K.M.R. van der Stam, E.D. van Ooijen, R. Meppelink, J.M. Vogels, and P. van der Straten. Large atom number Bose-Einstein condensate of sodium. *Review of Scientific Instruments*, 78:3102, January 2007.

[49] Z. Hadzibabic, C.A. Stan, K. Dieckmann, S. Gupta, M.W. Zwierlein, A. Gorlitz, and W. Ketterle. Two-Species Mixture of Quantum Degenerate Bose and Fermi Gases. *Physical Review Letters*, 88:160401, 2002.

[50] W. Demtröder. *Experimentalphysik 3.* Springer-Verlag GmbH, 2005.

[51] F.P. Schäfer. *Dye Lasers.* Springer-Verlag GmbH, 1977.

[52] C.V. Shank. Physics of Dye Lasers. *Rev. Mod. Phys.*, 47(3):649, Jul 1975.

[53] F.P. Schäfer, W. Schmidt, and J. Volze. Organic Dye Solution Laser. *Applied Physics Letters*, 9:306, oct 1966.

[54] Thieme Chemistry. *RÖMPP Online, Version 3.0* . Georg Thieme Verlag KG, 2007.

[55] Fuh R.A., Du H., Li J., Corkan A., and Lindsey J.S. PhotochemCAD: A Computer-Aided Design and Research Tool in Photochemistry. *Photochemistry and Photobiology*, 68:141, 1998.

[56] S Rabien. *Wirtsgalaxien von Quasaren und Der Laserleitstern für das Very Large Telescope.* PhD thesis, LMU, München, 2004.

[57] B. Lyot. Optical Apparatus with Wide Field Using Interference of Polarized Light. *C. R. Acad. Sci.*, 197:1593, 1933.

[58] S.M. Kobtsev and N.A. Sventsitskaya. Application of Birefringent Filters in Continuous-Wave Tunable Lasers: A Review. *Optics and Spectroscopy*, 73:114, jul 1992.

[59] H.J. Metcalf and P. van der Straten. *Laser Cooling and Trapping.* Springer-Verlag New York, Inc, 1999.

[60] A. Ashkin. Acceleration and Trapping of Particles by Radiation Pressure. *Phys. Rev. Lett.*, 24(4):156, Jan 1970.

[61] S. Chu, J.E. Bjorkholm, A. Ashkin, and A. Cable. Experimental Observation of Optically Trapped Atoms. *Phys. Rev. Lett.*, 57(3):314, Jul 1986.

[62] J.D. Jackson. *Klassische Elektrodynamik.* Gruyter, 2002.

[63] S. Chu, L. Hollberg, J.E. Bjorkholm, A. Cable, and A. Ashkin. Three-Eimensional Viscous Confinement and Cooling of Atoms by Resonance Radiation Pressure. *Phys. Rev. Lett.*, 55(1):48, Jul 1985.

[64] D.A. Steck. Sodium D Line Data. available at http://steck.us/alkalidata, 2003.

[65] M.A. Gehm. Properties of 6Li. extract from PhD thesis, 2003.

[66] P.D. Lett, R.N. Watts, C.I. Westbrook, W.D. Phillips, P.L. Gould, and H.J. Metcalf. Observation of Atoms Laser Cooled below the Doppler Limit. *Phys. Rev. Lett.*, 61(2):169, Jul 1988.

[67] J. Dalibard and C. Cohen-Tannoudji. Laser Cooling Below the Doppler Limit by Polarization Gradients: Simple Theoretical Models. *J. Opt. Soc. Am. B*, 6(11):2023, 1989.

[68] T. Walker, D. Sesko, and C. Wieman. Collective Behavior of Optically Trapped Neutral Atoms. *Phys. Rev. Lett.*, 64(4):408, Jan 1990.

[69] W. Ketterle, K.B. Davis, M.A. Joffe, A. Martin, and D.E. Pritchard. High Densities of Cold Atoms in a Dark Spontaneous-Force Optical Trap. *Phys. Rev. Lett.*, 70(15):2253, Apr 1993.

[70] Z. Hadzibabic, S. Gupta, C.A. Stan, C.H. Schunck, M.W. Zwierlein, K. Dieckmann, and W. Ketterle. Fiftyfold Improvement in the Number of Quantum Degenerate Fermionic Atoms. *Physical Review Letters*, 91(16):160401, October 2003.

[71] Z. Hadzibabic. *Studies of a Quantum Degenerate Fermionic Lithium Gas.* PhD thesis, Massachusetts Institute of Technology, 2003.

[72] M. Repp. Aufbau einer Vakuumapparatur für Experimente mit Ultrakalten Fermionischen und Bosonischen Quantengasen. Master's thesis, Kirchhoff-Institute for Physics, University of Heidelberg, 2007.

[73] J. Krieger. Title Undisclosed. Master's thesis, Kirchhoff-Institute for Physics, University of Heidelberg, 2008.

[74] Witte, A. and Kisters, T. and Riehle, F. and Helmcke, J. Laser cooling and deflection of a calcium atomic beam. *J. Opt. Soc. Am. B*, 9(7):1030, July 1992.

[75] A. Piccardo-Selg. Title Undisclosed. Master's thesis, Kirchhoff-Institute for Physics, University of Heidelberg, 2008.

[76] Z. Hadzibabic, S. Gupta, C.A. Stan, C.H. Schunck, M.W. Zwierlein, K. Dieckmann, and W. Ketterle. Fiftyfold Improvement in the Number of Quantum Degenerate Fermionic Atoms. *Physical Review Letters*, 91(16):160401, October 2003.

[77] M.O. Mewes, M.R. Andrews, N.J. van Druten, D.M. Kurn, D.S. Durfee, and W. Ketterle. Bose-Einstein Condensation in a Tightly Confining dc Magnetic Trap. *Phys. Rev. Lett.*, 77(3):416, Jul 1996.

[78] D.E. Pritchard. Cooling Neutral Atoms in a Magnetic Trap for Precision Spectroscopy. *Physical Review Letters*, 51:1336, October 1983.

[79] W. Petrich, M.H. Anderson, J.R. Ensher, and E.A. Cornell. Stable, Tightly Confining Magnetic Trap for Evaporative Cooling of Neutral Atoms. *Phys. Rev. Lett.*, 74(17):3352, Apr 1995.

[80] K.B. Davis, M.O. Mewes, M.R. Andrews, N.J. van Druten, D.S. Durfee, D.M. Kurn, and W. Ketterle. Bose-Einstein Condensation in a Gas of Sodium Atoms. *Phys. Rev. Lett.*, 75(22):3969, Nov 1995.

[81] J.P. Denschlag. *Kalte Atome in singulären Potentialen*. PhD thesis, University of Innsbruck, 1998.

[82] E.A. Donley, T.P. Heavner, F. Levi, M.O. Tataw, and S.R. Jefferts. Double-Pass Acousto-Optic Modulator System. *Review of Scientific Instruments*, 76(6):063112, 2005.

[83] F. Shimizu, K. Shimizu, and H. Takuma. Four-Beam Laser Trap of Neutral Atoms. *Optics Letters*, 16:339, mar 1991.

[84] C.G. Townsend, N.H. Edwards, C.J. Cooper, K.P. Zetie, C.J. Foot, A.M. Steane, P. Szriftgiser, H. Perrin, and J. Dalibard. Phase-Space Density in the Magneto-Optical Trap. *Phys. Rev. A*, 52(2):1423, Aug 1995.

[85] T. Ottenstein. A New Objective for High Resolution Imaging of Bose-Einstein Condensates. Master's thesis, University of Heidelberg, 2006.

Erklärung:

Ich versichere, dass ich diese Arbeit selbständig verfasst und keine anderen als die angegebenen Quellen und Hilfsmittel benutzt habe.

Heidelberg, den 20.11.2007

.....
(Unterschrift)